Urban Climate 66 (2026) 102858

Contents lists available at ScienceDirect

Urban Climate

journal homepage: www.elsevier.com/locate/uclim

Wind-driven chimney effect of vertical airflow induced by spatial patterns within the High-rise Tower-style Building

Junrui Mi [a], Zhenxin Liu [a,*], Chao Zhang [a], Wenqing Shi [b], Yuanyuan Zhang [a], Hong Liao [a]

[a] Jiangsu Key Laboratory of Atmospheric Environment Monitoring and Pollution Control, Jiangsu Collaborative Innovation Center of Atmospheric Environment and Equipment Technology, School of Environmental Science and Engineering, Nanjing University of Information Science and Technology (NUIST), Nanjing 210044, China

[b] School of Mechanical and Electrical Engineering, Beijing Institute of Graphic Communication, Beijing 102600, China

ARTICLE INFO

Keywords:
High-rise Tower-style Building(HRTB)
Cross-ventilation
Computational fluid dynamics (CFD) simulation
Chimney effect

ABSTRACT

While extensive research in atmospheric environmental modeling has clarified how urban morphology influences outdoor airflow and pollutant dispersion, the effect of internal spatial configuration on indoor ventilation remains underexplored. This study examines wind-driven airflow in High-rise Tower-style Buildings (HRTBs), focusing on spatial layouts that enable indoor–outdoor ventilation coupling. High-resolution CFD simulations with explicit internal structures and refined meshes were performed to resolve 3D airflow and vertical transport in the E/V shaft under different cross-ventilation scenarios. Results reveal that even without buoyancy effects, the E/V shaft structure inherently induces a strong upward velocity (U_z) that increases with height, forming a wind-driven chimney effect consistent with observations. Quantitative analysis shows that increasing the horizontal ventilation area from 10 m^2 to 16 m^2 (approximately 60%) enhances horizontal airflow by about 22%, while reducing the inter-floor kinematic pressure difference by roughly 5 m^2/s^2, this reduction decreases U_z by approximately 40%. In contrast, concentrating ventilation on lower floors (F1–F11) while sealing upper floors (F12–F33) increases U_z by nearly 50% and inter-floor kinematic pressure differences by about 10 m^2/s^2. These findings demonstrate that horizontal ventilation strategically alters the vertical pressure gradient, which in turn governs both the direction and magnitude of pollutant transport-including potentially pathogenic aerosols—through the building interior. From an applied perspective, we recommend compartmentalizing shafts, installing isolation doors, and optimizing exhaust openings to reduce pollutant and smoke transport. This study links indoor airflow with atmospheric transport principles, providing insights for improving air quality and environmental health in high-density urban areas.

1. Introduction

The indoor spatial pattern of a building influences interior airflow, thereby affecting indoor ventilation performance and air quality (Cui et al., 2021), with subsequent impacts on both the building's livability (Jia et al., 2021; Zaniboni and Albatici, 2022; Zhu et al.,

* Corresponding author.
E-mail address: liuzhenxin@nuist.edu.cn (Z. Liu).

https://doi.org/10.1016/j.uclim.2026.102858
Received 6 November 2025; Received in revised form 21 February 2026; Accepted 3 March 2026

2015) and its energy efficiency (Sha and Qi, 2020; Chen et al., 2020). Therefore, the influence of indoor space pattern on airflow field and pollutant transport diffusion has become a hot issue in atmospheric environment research. In addition, the transport diffusion of microscopic germs indoors is significantly affected by indoor spatial structure and airflow, which is also crucial for epidemiological studies (Han et al., 2024; Lyu et al., 2022); furthermore, indoor ventilation regimes significantly influence smoke dispersion dynamics and fire propagation during enclosure fires (Huang et al., 2019).

Over the past forty years, China's rapid urbanization has driven the proliferation of High-rise Tower-style Buildings (HRTBs), which now constitute one of the predominant residential building typologies in urban contexts. These structures typically comprise approximately 30 floors (denoted as F) and feature structurally complex internal layouts with high occupant density (Fu et al., 2022; Jo and Lee, 2006; Lu et al., 2009). Consequently, their ventilation design is of critical importance. In accordance with the national *Residential Project Code* (GB 55038–2025) (Ministry of Housing and Urban-Rural Development of the People's Republic of China, 2025), at least one vertically connecting area (e.g., elevator or ventilation shafts) is usually designed in HRTBs. In previous studies, it has been found that the presence of vertical zones improves the ventilation of the building interior and effectively promotes air flow, thus enhancing the indoor air exchange efficiency (Hang et al., 2023). Furthermore, in a CFD simulation study of a fire scenario in a HRTB (Zhang et al., 2008), it was found that the vertical velocity of the airflow within the vertical channels inside the building is closely related to the ventilation conditions of the rooms on each floor. Yang et al. (2013) quantitatively evaluated the airflow interactions between vertical ventilation shafts and adjacent spaces. Their results demonstrate that the inflow of warmer air from adjacent spaces into the shafts significantly enhances the building's overall ventilation.

In a HRTB fire incident in Nanjing, Jiangsu Province (Fig. 1), the fire originated on the ground floor but caused more severe damage on the upper floors (around the F23–F33) than on the middle floors (around the F9–F20), as shown in Fig. 1(a). This anomalous vertical spread was likely influenced by the building's vertically connected rooftop structure (Fig. 1(b)), where strong upward airflows may have carried burning debris or embers upward, igniting combustible materials stored on the upper floors.

In the past, atmospheric ventilation processes both inside and around urban buildings have remained a central topic in the fields of building environmental science and atmospheric science(van Hooff and Blocken, 2010; Toparlar et al., 2017; Huang et al., 2025). Extensive studies based on atmospheric environment modeling have systematically demonstrated how building exterior morphology, street-canyon geometry, and their spatial configurations govern outdoor airflow structures and pollutant dispersion processes, providing a solid theoretical basis for understanding ventilation characteristics at the urban and neighborhood scales(Nascimento et al., 2025; Allegrini and Carmeliet, 2017; Gao et al., 2018; Guo et al., 2025; Deng et al., 2024). Meanwhile, existing studies have widely addressed indoor airflow and ventilation performance, particularly in relation to atria, room-scale geometries, and building envelope openings, providing detailed insights into airflow organization and ventilation efficiency in indoor environments(Jian et al., 2024; Fallahpour et al., 2024; Jiang et al., 2023). It should be noted that most existing studies on indoor ventilation primarily adopt single rooms or localized spaces as their analytical units, with research efforts largely concentrated on relatively isolated ventilation domains or idealized indoor configurations. From the perspectives of opening location, number, and area, these studies have systematically examined the influence of building envelope features on indoor airflow patterns and ventilation performance, offering valuable insights into ventilation mechanisms at the local spatial scale(Fu et al., 2024; Zhang et al., 2022; Montazeri, 2011; Qiu et al., 2023; Hu et al., 2024).

However, for HRTBs, which represent a prevalent urban residential form, the internal spatial organization is typically characterized by complex three-dimensional configurations composed of elevator shafts, corridors, and multistory vertically connected spaces. These internal elements do not function independently; instead, they are interconnected through both vertical and horizontal pathways, forming integrated indoor airflow networks whose organization fundamentally differs from that of single-room or localized ventilation units(Ray et al., 2014; Liu et al., 2009; Fini et al., 2016). For example, numerous studies have examined airflow and ventilation in more

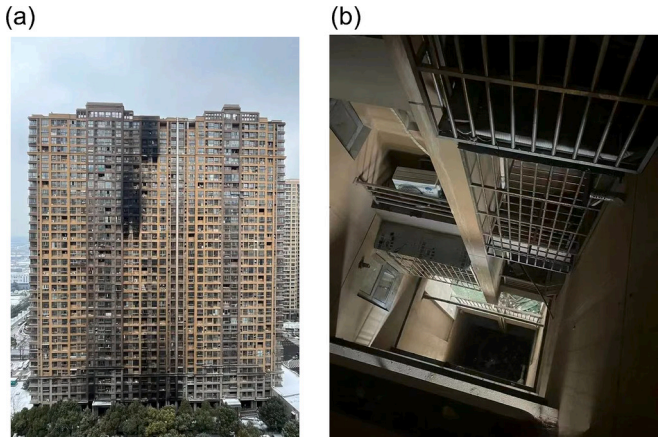

Fig. 1. In February 2024, a fire broke out in a neighborhood in Yuhuatai District, Nanjing, Jiangsu Province, China, caused by the spontaneous combustion of an electric car on the ground floor; however, the fire eventually spread upwards and burned more severely on the higher floors ($F > 21$) than the middle floors ($9 < F < 21$), (a): Overview of building damage after the fire, (b): Elevator shaft inside the building.

localized spaces, such as atria, individual rooms, and building envelope openings, highlighting the influence of room geometry and opening configurations on airflow patterns and ventilation efficiency (Zhang et al., 2022; Lin et al., 2025; Gao et al., 2011).

In this context, high-fidelity three-dimensional building geometry modeling combined with computational fluid dynamics (CFD) simulations provides an effective methodological framework for investigating indoor airflow organization from a whole-building spatial configuration perspective, particularly for HRTBs(Zhu et al., 2015; Jo and Lee, 2006; Arpino et al., 2023; Cheung and Liu, 2011). Zhang et al. (2022) conducted a simple modeling of a room and explored the effect of different opening configurations on trans-ventilation through CFD simulations, and found that two opening configurations significantly outperformed a single opening configuration in terms of improving ventilation rates. And a related study by (Shetabivash, 2015) also verified that the indoor cross-ventilation conditions of a building are significantly affected by the location and area of the room openings. Another study quantitatively assessed the role of different air supply rates inside actual buildings in affecting indoor atmospheric aerosol distribution (Zhai et al., 2011). A substantial body of literature, conversely, has prioritized the outdoor urban scale(Shirzadi et al., 2021; Liu et al., 2025a; Merlier et al., 2018; Chen et al., 2023; Kastner and Dogan, 2023). Still more studies have focused on the spatial scale of neighborhoods/complexes, where the spatial distribution of buildings affects the spatial and temporal characteristics of outdoor atmospheric flow fields. (Chen et al., 2020; Abd Razak et al., 2013; Adelia et al., 2019; Allegrini, 2018; Antoniou et al., 2017; Fang et al., 2021; Hsieh and Huang, 2016; Liu et al., 2022) used a CFD-RANS simulation-based approach to simulate the air pollution situation of an entire urban area of a city in Spain, especially the spatial and temporal distribution characteristics of the important air pollutant NO_X concentration. Jing et al. (2021) proposed an idealized high Reynolds number porous media city model combined with a CFD approach to quantify the breathability of urban ventilation. However, the above studies focus more on completely outdoor or indoor environments, for example, when CFD simulations are conducted for indoor airflow fields, the outdoor background wind field is often simplified to the boundary conditions of the internal surfaces of the building or vents such as windows and doors in the simulation setup. In addition, the modeling of the spatial structure of the building is simplified, especially for the simulation of large airflow field in outdoor open space, the building model often only has a relatively brief outline of the external surface characteristics, not only do not take into account the influence of the more detailed structure of the airflow, but also basically ignored characteristics of the airflow through the building inside and outside the formation of the flow field. This simplification often neglects the critical coupling between the internal layout of buildings and the external wind field, a gap particularly relevant for understanding airflow in vertically complex HRTBs.

There are also some studies that use complex building models to achieve better environmental simulation results. Yamamoto et al. (2021) proposed a method combining heat transfer simulation (HTS), CFD, and a two-dimensional heat flow tool (Hygrabe2D) to overcome the limitations of traditional HTS in handling complex building shells (e.g., radial-shaped buildings). By coupling multiple simulation tools, the study improves the accuracy of thermal environment calculations and successfully evaluates the annual average temperature of the building and the internal temperature of the shell. Nevers et al. (2024) introduced an artificial porosity approach combined with a CFD method to simulate the wind environment of buildings, utilizing permeability (Darcy term) and inertia (Forchheimer term) to simulate complex "lift-up buildings". The study shows that the model can effectively simulate the wind environment of buildings. It is shown that the model is able to effectively simulate the airflow pattern at the open ground underneath the building with low computational cost. Kahsay et al. (2019) conducted CFD simulations using buildings with complex exterior architectural elements, such as balconies and external shading devices, to investigate the influence of these components on the convective heat transfer coefficient (CHTC). The exterior architectural elements were found to significantly affect the local and surface-averaged CHTC values of the building. Younes and Abi Shdid (2013) explored the effect of air leakage in the building envelope on the building energy consumption using a three-dimensional multi-physics hygrothermal simulation model that realistically represents the cracks in the building envelope, including the shape, location, and number of cracks in the building shell, and various climatic conditions were taken into account in the simulation process, which significantly improved the accuracy of the calculation of the air leakage heat load. While these studies advance the modeling of building exteriors and envelopes, they do not centrally address how the internal spatial configuration of a building, such as the layout of shafts and floors in an HRTB, governs the internal flow field and its interaction with the outside wind.

This study selects a representative unit block from the HRTB shown in Fig. 1 and performs three-dimensional spatial modeling, including ventilation windows, indoor space layout, and vertically continuous structures (E/V shaft) on each floor, such as elevator shafts, atria, or other vertically connected internal spaces. The geometric abstraction of the E/V shaft reflects common features of existing HRTBs: corridors on each floor connect to resident-facing openings, forming a vertically continuous space that provides potential pathways for wind-driven vertical airflow. Each floor is connected to the E/V shaft through assumed openings, representing windows, balcony doors, or partially open corridor doors, while the internal spaces are also coupled to the external environment via façade openings, establishing indoor–shaft–outdoor airflow connectivity. For modeling efficiency, 2–4 households per floor are simplified into a single connected floor unit, preserving the main airflow mechanisms while reducing computational cost. The outdoor open space is set up in OpenFOAM mode with a typical background wind speed field, where the wind is horizontally uniform and varies with height according to the logarithmic law(Masson, 2000). The external airflow enters the building's interior through windows on each floor and openings on the rooftop. The simulation ultimately yields the spatial distribution characteristics of the airflow field around the HRTB perimeter, inside each floor, and within the vertical rooftop structure. Furthermore, the indoor and outdoor cross ventilation performance is adjusted by changing the ventilation area of the windows in the mode setting, and the vertical indoor airflow modes are investigated with numerical sensitivity.

In this study, four different scenarios (Table 1) are set up to investigate the effects of changing the ventilation conditions of different floors on the airflow patterns inside the vertical zone. In particular, in one of the simulation scenarios (L10), windows are opened on the windward and leeward sides of the lower floors and sealed on the middle and upper floors, similar to the situation where the initial fire point is located on the lower floors of a building and the lower floors of the building have been burned out after a period of time

after the fire has occurred. The simulation results of this scenario would be helpful to further verify the influence of the structural characteristics of the building and the variation of indoor and outdoor wind fields on the fire smoke or other air pollutants propagation path.

This study is of great value in guiding the design of future urban habitat buildings, assessing and improving indoor air environments, as well as key issues in the fields of science and applications such as emergency mitigation and disease prevention.

2. Model and methodology

2.1. Model description and domain settings

In this study, a representative HRTB commonly found in urban areas was selected as the prototype, and a three-dimensional computational model was developed to describe its complex internal and external spatial configuration. The geometric dimensions and spatial parameters of the model were defined with reference to the national *Residential Project Code* (GB 55038–2025) (Ministry of Housing and Urban-Rural Development of the People's Republic of China, 2025), ensuring consistency with current residential building design specifications in China. The computational model does not aim to reproduce a specific real-world building, but rather constitutes an engineering-oriented abstraction of a class of HRTBs that are widely present in Chinese cities. During the abstraction process, key structural features shared by typical high-rise residential buildings were retained, including a regular floor plan, representative floor-to-floor heights, façade openings, and vertically continuous internal spaces extending across multiple stories, such as atrium-style ventilation shafts or non-fully enclosed elevator/vertical (E/V) shafts. Such vertically connected spaces are commonly observed in existing high-rise residential buildings, particularly those constructed under earlier design practices, with higher floor area ratios, or incorporating atrium-based vertical spatial organization. This geometric abstraction effectively captures the dominant vertical airflow pathways within the building, providing a representative computational framework for investigating wind-driven vertical airflow and associated chimney effects.

The model has 33 floors with a height of 3.1 m. There is a rooftop at the top of the building with a height of 3 m. Together with the accessory structures, the total height of the model is about 105 m. Each floor has a length of 15.4 m and a width of 13.5 m, and the total area of a single floor is approximately 200 m^2, which is in line with the layout of a typical residential house type. The three-dimensional architectural model in this study was based on the building depicted in Fig. 1. However, to enhance the generality of the conclusions and reduce modeling and computational complexity, decorative elements and occupant-installed auxiliary structures were deliberately simplified or omitted. This abstraction allows the model to capture the essential thermal and airflow behaviors of this building typology, without being influenced by site-specific or non-representative features. Consequently, the results are expected to provide broadly applicable insights for buildings of this type, rather than being constrained to a single, unique case. The spatial layout of the interior of each floor and the location of the stairs/elevator shafts in the floor are shown in Figs. 2(a-c), and the structural shape of the whole building is shown in Figs. 2(d-g). In the model, each floor is connected to the vertical E/V shaft through assumed openings, representing resident-facing windows, balcony doors, or partially open corridor doors. Meanwhile, the internal spaces connect to the external environment via facade windows. Thus, the so-called “open boundary” refers to the building's coupling with the external atmosphere, rather than the atrium being directly open to the outdoors. This indoor–shaft–outdoor connectivity is a key feature captured by our simulations. Furthermore, an unstructured mesh is generated in OpenFOAM to accurately capture the complex geometries both inside and outside the building for subsequent CFD simulations of airflow. Non-uniform unstructured grids were employed to accommodate the complex geometries encountered. Specifically, the indoor domains—including rooms, stairwells, elevator shafts, and other enclosed spaces—are meshed with an average spatial resolution of approximately 0.1 m to resolve fine-scale flow structures. In contrast, the outdoor open areas are discretized with a coarser resolution of 2 m. This meshing strategy achieves a balance between computational efficiency and the fidelity required for resolving critical flow features.

In this study, four sets of scenarios with varying numerical sensitivities are established in the OpenFOAM model to investigate the impact of cross-ventilation performance on the vertical indoor airflow patterns. For modeling efficiency, 2–4 households per floor are simplified into a single connected floor unit, focusing on the core mechanism of vertical airflow induced by horizontal wind and floor-to-shaft connectivity. While this does not reflect all detailed architectural features, it allows a systematic investigation of the wind-driven chimney effect without unnecessary computational burden. Specifically, different window opening areas are configured on the windward and leeward facades in each scenario, while the two side windows are uniformly set with an opening area of 3 m^2, according to the real view in Fig. 1. These configurations enable a systematic analysis of how asymmetries in facade openings influence

Table 1
Three-dimensional model setup for four simulation scenarios.

simulation scenario	LF (m^2)	MF (m^2)	UF (m^2)
A10	10	10	10
A16	16	16	16
L10	10	0	0
UP10	0	0	10

Note. LF: window areas in the lower floors; MF: window areas in the middle floors; UF: window areas in the upper floors, the designation “UP10” is used to indicate openings on the upper floors and is chosen to avoid confusion with the conventional wind velocity *U*.

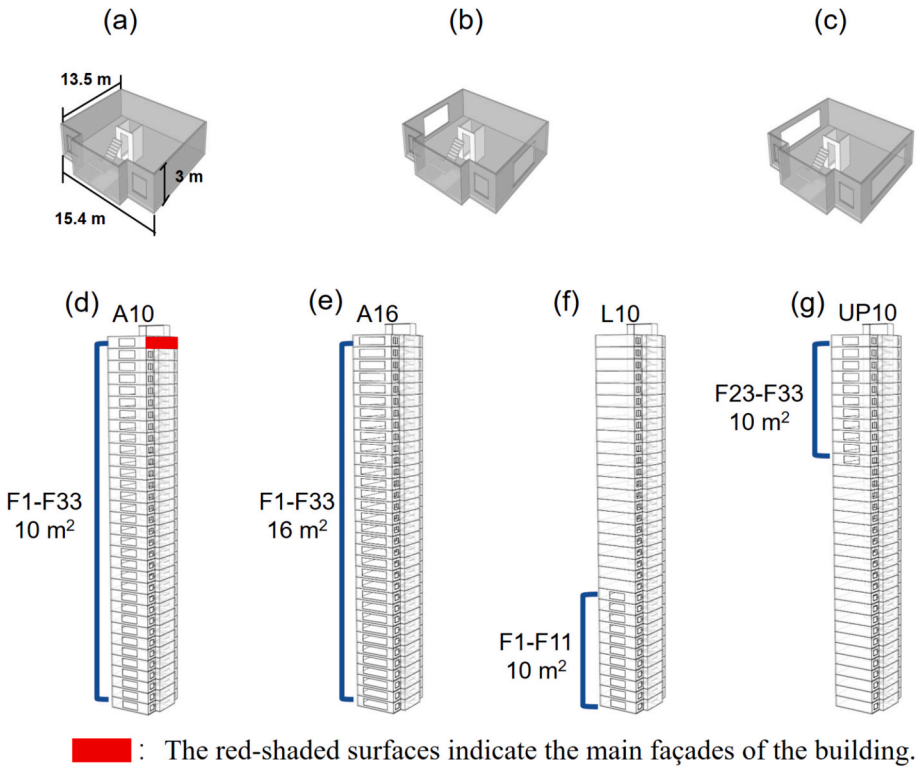

Fig. 2. In the HRTB models, all floors share identical internal and external geometries. The study investigates four ventilation scenarios, defined by variations in windward and leeward window areas and their distribution across different floors, (a) minimum ventilation - no windows on windward/leeward sides; (b) normal ventilation −10 m^2 windows (2 m × 5 m) on both sides; (c) super ventilation −16 m^2 windows (2 m × 8 m) on both sides; (d-g) are shown to represent the models and settings used in four scenarios (A10, A16, L10, UP10).

indoor–outdoor airflow interactions and the resulting vertical ventilation modes. In the following, we name these four scenarios as A10, A16, L10, and UP10, respectively, and set the parameters of the scenarios in Table 1, and set the initial boundary conditions of the model in Table 2. In the scenarios, the amount of cross ventilation on each floor of the whole building is set to 10 m^2 (for A10) or 16 m^2 (for A16) to represent the normal and super ventilation states. In the other two sets of scenarios, the middle and upper floors (for L10) and the middle and low floors (for UP10) are set to be in the low ventilation state, i.e., the windward and leeward facades on these floors are configured with a ventilation window area of 0 m^2, while the rest of the floors are kept in the normal ventilation state (i.e. 10 m^2). Here, the lower floor includes F1-F11, the middle floor refers to (F12-F22), and the upper floor refers to (F23-F33). It is worth noting that the observational conditions could not be perfectly synchronized with the simulated ventilation settings. In the numerical scenarios, window openings were prescribed strictly according to the configurations described above. However, during field observations, it was impractical to reproduce these settings exactly. Instead, corresponding observation periods were selected to approximate the modeled conditions. For example, when outdoor temperatures were high and residents tended to keep windows closed and use air conditioning, the situation resembled the low-ventilation scenarios. Conversely, during periods of mild temperature, low humidity, and good air quality, residents were more inclined to open windows, which corresponded to the normal or enhanced ventilation scenarios. In some cases, coordination with residents and property management was sought to adjust window openings on selected floors during specific time slots, so as to best match the ventilation configurations illustrated in the four modeled scenarios.

2.2. CFD model description

This study employs the OpenFOAM computational fluid dynamics (CFD) framework to simulate airflow fields. The numerical

Table 2
Initial simulation parameters.

Wind Speed(m/s)	Wind Direction	k ($kg{\cdot}m^2/s^2$)	ε_0 (m^2/s^3)	μ (kg/(m•s))
5	90°(east)	1.5	0.0301	1.5×10^{-5}

Note. k: turbulent kinetic energy; ε_0: initial turbulent dissipation rate; μ: aerodynamic viscosity.

methodology incorporates a pressure-based steady-state solver (simpleFoam), the standard $k-\varepsilon$ turbulence model, and carefully selected near-wall treatments and mesh configurations appropriate for the physical scale and objectives. The selection of a steady-state RANS formulation stems from the primary focus on time-averaged flow characteristics under fixed boundary conditions (e.g., constant wind velocity/direction), rather than transient phenomena. This approach significantly enhances computational tractability for large domains while capturing equilibrium flow behavior. Under the investigated conditions, the airflow is predominantly driven by external wind pressure and remains within a low-Mach-number regime. As a result, compressibility effects and thermal buoyancy are negligible and are not explicitly considered. Within this context, the incompressible Reynolds-averaged Navier–Stokes (RANS) equations provide a physically consistent description of the dominant wind-driven ventilation processes(van Hooff et al., 2017; Liu et al., 2025).

Based on this governing equation system, a pressure-based steady-state formulation is adopted, in which pressure serves as the primary variable coupling continuity and momentum equation. This formulation naturally leads to solving a kinematic pressure field rather than the absolute thermodynamic pressure, which is particularly suitable for incompressible flow solvers and facilitates numerical stability and efficiency. Accordingly, the specific pressure definition and solution procedure adopted in simpleFoam are detailed below.

The robust SIMPLE algorithm within simpleFoam efficiently solves the incompressible RANS equations. In this framework, the kinematic pressure (p) $p = P/\rho$ is solved directly, where P is the thermodynamic (absolute) pressure and ρ is the constant fluid density. The kinematic pressure has dimensions of m^2/s^2 and represents the relative pressure field used internally by the incompressible solver, rather than an absolute pressure, equivalent to the unit of specific kinetic energy, allowing direct comparison and combination with flow kinetic energy in Bernoulli-like formulations. For incompressible flows, solving kinematic pressure rather than absolute pressure improves numerical stability and convergence in the SIMPLE pressure-velocity coupling.

The resulting pressure field is defined relative to a reference value (p_0), such that regions where p exceeds the reference are positive, while regions below the reference are negative, reflecting local deviations from the imposed baseline. This formulation ensures physically consistent and numerically stable solutions, facilitating robust simulation of large airflow domains under complex boundary conditions.

Accordingly, this study employs the kinematic pressure field (p, in m^2/s^2) for analysis, which directly characterizes the dynamic state of airflow rather than static or absolute pressure values. For instance, within the E/V shaft, a decrease of 1 m^2/s^2 in the kinematic pressure (p) corresponds to a decrease of approximately 0.012 hPa in the static pressure, assuming an air density of 1.2 kg/m^3. This form of pressure representation facilitates a clearer depiction of the spatial distribution of local pressure gradients and their coupling with the vertical airflow field, thereby elucidating the underlying dynamic mechanisms governing airflow in vertically connected spaces.

2.2.1. *Turbulence closure scheme*

In this study, a second-order semi-closed scheme for turbulence based on the Reynolds time-averaged method and $k-\varepsilon$ theory is developed for parameterizing the spatial distributions of atmospheric turbulence modes, turbulent kinetic energy, and turbulence dissipation at street-valley scales and inside and outside buildings. The scheme ignores the intermittent nature of turbulence in the time dimension and directly generates a steady-state turbulent spatial field based on Reynolds time-averaging. Under this assumption, the turbulent eddy spatial distribution is isotropic in nature and uniformly stable in the time dimension. The turbulence dissipation scale is further generated based on the $k-\varepsilon$ theory and the scale spectrum of turbulent energy is obtained. Thus, the arithmetic is simplified while considering the main features of turbulence. The continuity and momentum equations are given by Eqs. (1–2).

$$\frac{\partial \rho}{\partial t}+\frac{\partial}{\partial x_i}(\rho u_i)=0 \tag{1}$$

$$\frac{\partial}{\partial t}(\rho u_i)+\frac{\partial}{\partial x_j}(\rho u_j u_i)=-\frac{\partial p}{\partial x_i}+\frac{\partial \sigma_{ij}}{\partial x_j}+\frac{\partial}{\partial x_j}\left(-\rho\overline{u_i' u_j'}\right) \tag{2}$$

u_i is the Reynolds-averaged velocity component, ρ is the fluid density, u_i' is the fluctuating velocity, and σ_{ij} is the component of the stress tensor. The equations for turbulent kinetic energy (k) and its dissipation rate (ε) are given as follows:

$$\frac{Dk}{Dt}=\frac{\partial}{\partial x_j}\left[\left(\nu+\frac{\nu_t}{\sigma_k}\right)\frac{\partial k}{\partial x_j}\right]+\nu_t\left(\frac{\partial u_i}{\partial x_j}+\frac{\partial u_j}{\partial x_i}\right)\frac{\partial u_i}{\partial x_j}-\varepsilon \tag{3}$$

In the Eq. (3), $\frac{D}{Dt}=\frac{\partial}{\partial t}+u_j\frac{\partial}{\partial x_j}$ represents the material derivative, while $\nu=\frac{\mu}{\rho}$ corresponds to the kinematic viscosity.

$$\frac{D\varepsilon}{Dt}=\frac{\partial}{\partial x_j}\left[\left(\nu+\frac{\nu_t}{\sigma_\varepsilon}\right)\frac{\partial \varepsilon}{\partial x_j}\right]+C_1\frac{\varepsilon}{k}\nu_t\left(\frac{\partial u_i}{\partial x_j}+\frac{\partial u_j}{\partial x_i}\right)\frac{\partial u_i}{\partial x_j}-C_2\frac{\varepsilon^2}{k} \tag{4}$$

In the governing equations, C_μ、C_1、C_2、σ_k and σ_ε are empirical constants of the standard $k-\varepsilon$ turbulence model. These parameters are typically determined through calibration against representative experimental datasets and benchmark case studies. In the present study, the adopted values are $C_\mu = 0.09$, $C_1 = 1.44$, $C_2 = 1.92$, $\sigma_k = 1.00$, and $\sigma_\varepsilon = 1.30$.

It is important to note that the model introduces the turbulent viscosity coefficient ν_t which also requires parameterization, as shown in Eq. (5):

$$\nu_t = C_\mu \frac{k^2}{\varepsilon} \tag{5}$$

Where C_μ is the empirical parameter of the model. Although this study aims for a steady-state flow solution (assuming flow variables are statistically time-independent , $\frac{\partial}{\partial t} = 0$), the time derivative terms are retained in the governing Eqs. (1)–(4). This is primarily for two reasons. First, these equations represent the most general mathematical formulation of the Reynolds-averaged Navier-Stokes equations and the associated turbulence model, of which the transient terms are an integral part. Second, in the numerical solution procedure, we employ an iterative algorithm based on "pseudo-time" marching (e.g., SIMPLEC). Within this framework, the time derivatives do not represent physical time evolution but act as a numerical driver that advances the solution vector toward a steady state. Starting from an initial flow field, the solution is progressively updated under fixed boundary conditions via pseudo-time steps until the changes in flow variables (residuals) fall below a convergence criterion. At that point, the solution ceases to change with (pseudo-)time, the time derivatives effectively vanish, and the final result obtained satisfies the steady-state RANS equations. Thus, retaining the time terms both preserves the completeness of the equations and accurately reflects our numerical solution path for obtaining a steady-state solution.

The initial values of k and ε are determined based on Eq. (6) and Eq. (7), respectively.

$$k = \frac{3}{2}\left(I\left|U_{ref}\right|\right)^2 \tag{6}$$

$$\varepsilon = \frac{C_\mu^{0.75} k^{1.5}}{l} \tag{7}$$

In Eqs. (6) and (7), k is the turbulent kinetic energy, I is the turbulence intensity, U_{ref} is the reference velocity, and l is the turbulence length scale.

2.2.2. Near-wall grid and modeling settings

Since the $k-\varepsilon$ model is primarily applicable to high Reynolds number flows, its accuracy deteriorates in near-wall regions where turbulence remains underdeveloped and the Reynolds number is relatively low. Direct application of the $k-\varepsilon$ model in these regions may lead to significant errors; therefore, an improved turbulence treatment is required near the wall. A single shear force governs the near-wall region, and the relationship between turbulent kinetic energy (k), turbulence dissipation rate (ε), and friction velocity ($u_\tau = \sqrt{\tau_w/\rho}$, τ_w is the wall shear stress , ρ is the fluid density) is formulated using a semi-implicit expression. The damping effect of the wall on turbulence development depends on the wall-normal distance, leading to the following expression:

$$u^+ = \frac{\ln E y^+}{\kappa} \tag{8}$$

In Eq. (8), E and κ are constants, typically taken as 9.8 and 0.4, respectively. u^+ ($u^+ = U/u_\tau$, U being the local velocity) represents the dimensionless velocity, and y^+ ($y^+ = y u_\tau/\nu$, y being the wall-normal distance and ν the molecular kinematic viscosity) denotes the dimensionless wall-normal distance of a grid point. When $y^+ > 30$, the near-wall region follows the logarithmic law described by Eq. (8). Under the assumption that turbulence production and dissipation are balanced within the logarithmic region near the wall, the dimensionless formulation is given by:

$$u^+ = \frac{u C_\mu^{0.75} k^{0.5}}{\tau_w/\rho}, y^+ = \frac{\rho C_\mu^{0.25} k^{0.5} y}{\nu} \tag{9}$$

In Eq. (9), τ_w represents the wall shear stress, and ν is the air viscosity. In practical calculations, when $y^+ > 30$, the wall follows the logarithmic function law.

The SIMPLE (Semi-Implicit Method for Pressure-Linked Equations) algorithm in OpenFOAM is then employed as the solver, and a second-order discretization scheme is used to solve all convective and viscous terms in the governing equations.

For the entire simulation domain, boundary conditions were rigorously prescribed in the initial field files (under the directory named by "0"). The velocity field (U) was configured with the following boundary conditions: The east boundary was specified as a fixedValue inlet, with the incoming wind velocity defined by a logarithmic profile based on the atmospheric boundary layer. Within the height range of the target building, the selected profile exhibits relatively small variation with height and overall displays weak vertical shear. Therefore, over the building-scale domain of interest, the inlet flow can be approximated as quasi-uniform. This setup is intended to minimize the influence of externally imposed vertical shear on the flow field, thereby more clearly highlighting the vertical airflow features induced by the building's intrinsic spatial configuration, particularly the vertically connected E/V shaft and the wind-driven vertical transport mechanism between the shaft and floor openings; the west boundary was pressureInletOutletVelocity as the outlet; the north and south boundaries were zeroGradient; all building surfaces and the ground applied noSlip conditions; and the front/back planes were set to zeroGradient.

Concurrently, the pressure field (p) enforced total pressure specification (totalPressure) at the west boundary with reference pressure $p_0 = 0\ Pa$ and specific heat ratio $\gamma = 1.4$, while consistently applying zero-gradient Neumann conditions (zeroGradient) at north, south, east, ground, front/back planes, and all building surfaces to satisfy $\nabla p \cdot n = 0$ compatibility requirements. The kinematic pressure values within the domain are therefore defined relative to this reference: regions with p above the reference are positive,

whereas regions with p below the reference are negative, reflecting local deviations from the imposed total pressure baseline.

This configuration ensured physical consistency through the Rhie-Chow coupled pressure-velocity formulation, as validated by mass conservation (net flux variation $< 0.1\%$) and aerodynamic force drag coefficient stabilization ($\Delta C_D/\Delta t < 0.5\%$) across 1000 iterations.

The steady-state simulation employed a pseudo-transient approach with a fixed time step of $\Delta t = 1\ s$ over 5000 iterations, starting at $t = 0\ s$ (startTime) and ending at $t = 5000\ s$ (endTime). Data were output every 500 timesteps (writeInterval) under a time-step-controlled condition (writeControl). This configuration enabled detailed temporal monitoring of convergence behavior while maintaining computational efficiency through restart capabilities from the latestTime.

Steady-state convergence was rigorously attained when simultaneously satisfying dual criteria: (a) iterative residuals met prescribed numerical thresholds, with pressure (p) and velocity (U) linear solvers achieving absolute tolerances of 1×10^{-6} (relative tolerance 0.1) at each SIMPLE cycle, while global residual controls enforced termination only after initial p and U residuals fell below 1×10^{-4} consecutively; and (b) key physical quantities – including system pressure drop (Δp), boundary mass flow rates (m), and aerodynamic coefficients (Lift Coefficient C_L and Drag Coefficient C_D) – stabilized within 0.1% variation over 50 consecutive iterations, thereby ensuring both numerical consistency and physical stationarity for engineering-relevant solutions. This hierarchical approach, employing stricter linear solver tolerances (1×10^{-6}) than global residual thresholds (1×10^{-4}), maintained computational robustness while aligning with established high-fidelity simulation practices (Li et al., 2019; Huang et al., 2011).

2.2.3. *Generation of discretized grid and grid independence analysis*

Fig. 3 shows the computational domain and mesh configuration employed in the CFD simulations(Tominaga et al., 2008). To ensure that the numerical results were not affected by mesh discretization, a Grid Independence Test (GIT) was conducted. Under identical computational domain extents, boundary conditions, and physical models, three sets of unstructured meshes with different spatial resolutions were generated by adjusting the refinement levels of refinementSurfaces and refinementRegions in the snappyHexMeshDict file.

In the three mesh configurations, the refinement level of the building surfaces was set to level (22) for the coarse grid, with an E/V shaft box refinement level of 1. For the medium grid, the building surface refinement was set to level (33) and the E/V shaft box refinement to 2. For the fine grid, the refinement levels were increased to level (4 4) and 3, respectively, for the building surfaces and E/V shaft box.

The total cell counts were approximately 0.58 million (coarse), 1.88 million (medium), and 6.20 million (fine). As the refinement level increased, the mesh density and overall spatial resolution improved substantially.

To effectively capture the complex flow characteristics within the building, a vertical section inside the E/V shaft was selected as the key analysis region. The velocity (U) and pressure (p) profiles obtained from different mesh resolutions were compared. This region features pronounced velocity gradients and intricate flow structures, making it highly sensitive to mesh refinement and suitable for assessing the adequacy of the mesh configuration.

Furthermore, to quantitatively evaluate the sensitivity of the numerical results to mesh resolution, the Grid Convergence Index (GCI) method was employed to verify and quantify the convergence behavior among the different mesh densities.

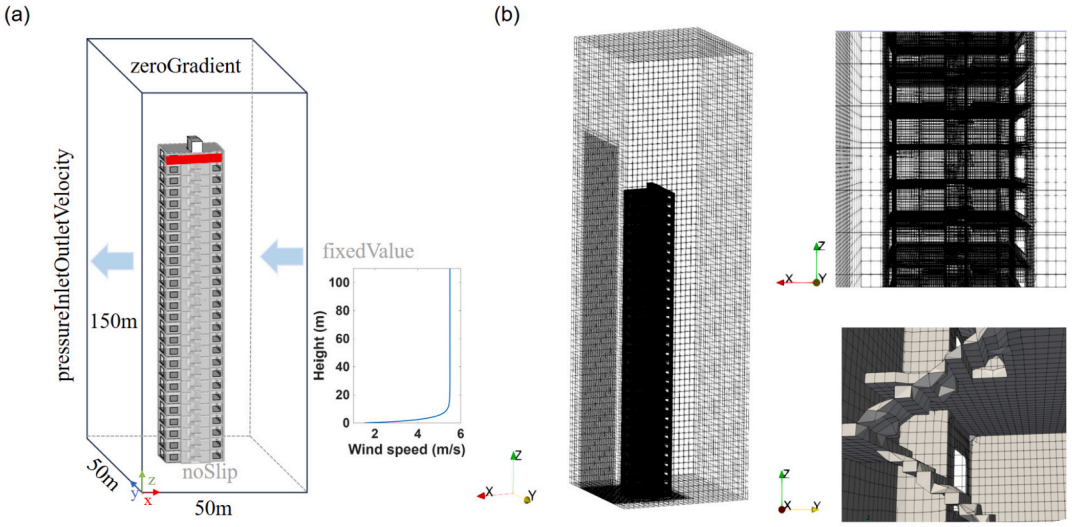

Fig. 3. (a) Computational domain used in the simulation; (b) grid arrangement of A10.

$$r = \frac{h_i}{h_j} \tag{10}$$

In Eq. (10), h represents the characteristic mesh size, defined as the mean dimension derived from the cell volume. To assess the sensitivity of the results to mesh resolution, the relative solution difference between mesh levels i and j was computed using Eq. (11).

$$\varepsilon = \frac{\varphi_i - \varphi_j}{\varphi_j} \tag{11}$$

In Eq. (11), φ represents the simulated value of either velocity (U) or pressure (p) at the key monitoring point. According to the definition proposed by Roache (Roache, 1997) the Grid Convergence Index (GCI) is expressed as follows:

$$GCI_{ij} = F_s \frac{|\varepsilon|}{r^p} \tag{12}$$

In Eq. (12), F_s denotes the safety factor, which is set to 1.25 when three mesh levels are used for sensitivity analysis. The parameter p represents the theoretical order of accuracy of the numerical scheme. In this study, a second-order discretization scheme (such as Gauss linear and linearUpwind) was employed, and therefore $p = 2$.

The GCI value indicates the percentage of relative error between two mesh levels and serves as an indicator of mesh independence. A smaller GCI value (typically less than 5%) suggests that the numerical results have approached convergence with respect to mesh refinement, and the simulation outcomes are not significantly dependent on the grid resolution.

Figs. 4(a-b) show the vertical profiles of simulated wind velocity (U) and pressure (p) within the E/V shaft under different mesh resolutions, while Figs. 4(c–d) show the Grid Convergence Index (GCI) calculated based on the U and p results. The results indicate that, when using the medium and fine meshes, the relative errors of both U and p remain within 5%, whereas the GCI values for the medium–coarse mesh comparison range from 5% to 20%. Deviations in the coarse-mesh results begin to emerge at heights of approximately 30–40 m and further increase above 70 m. Since the GCI values between the medium and fine meshes are generally below 5%, the numerical solutions can be considered to have effectively converged with mesh refinement. Considering both computational accuracy and cost efficiency, the medium-resolution mesh was ultimately selected for subsequent simulations.

2.3. Source and analysis method of observation data

Fig. 5(b) illustrates the spatial distribution of observation points inside the E/V shaft, including those at the shaft exit. Fig. 5(a) presents the wind rose for Nanjing City during May–June 2023, showing that easterly and southerly winds were predominant during this period, with typical wind speeds between 3 and 7 m/s. In accordance with these observed meteorological conditions, the wind speed boundary condition in the simulation was set to 5 m/s, with a southerly wind direction.

Validation of the simulated vertical wind velocity (U_z) and kinematic pressure (p) was performed using in situ measurements of vertical wind velocity and ambient (static) pressure (P), conducted at the rooftop exit (Fig. 1) and inside the E/V shaft. A Kanomax 6006-DE Anemomaster was used for wind velocity measurements, offering a resolution of 0.01 m/s with high linearity and stability, which makes it suitable for detecting subtle vertical airflows. Static pressure was measured with an ICP-1011 MEMS barometric sensor, covering a range of 300–1100 hPa with an absolute accuracy of ±1 Pa and a resolution of approximately 0.4 Pa. This sensor also provides a sufficiently fast dynamic response to capture minor pressure fluctuations in the E/V shaft. Both instruments enable high-

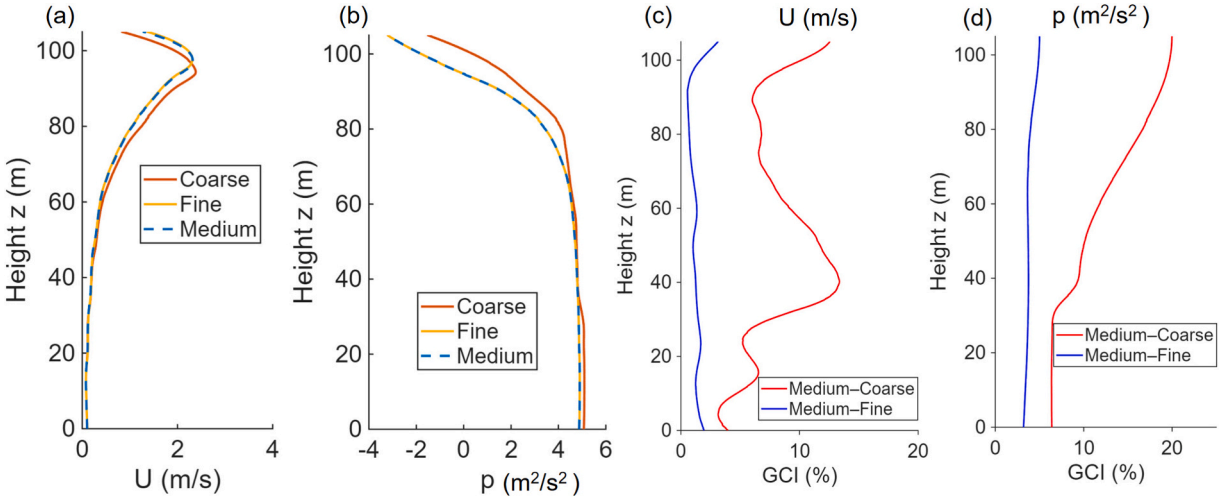

Fig. 4. (a-b) Vertical profiles of velocity (U) and pressure (p)inside the E/V shaft under different grid resolutions and mesh densities; (c-d) corresponding GCI values for U and p.

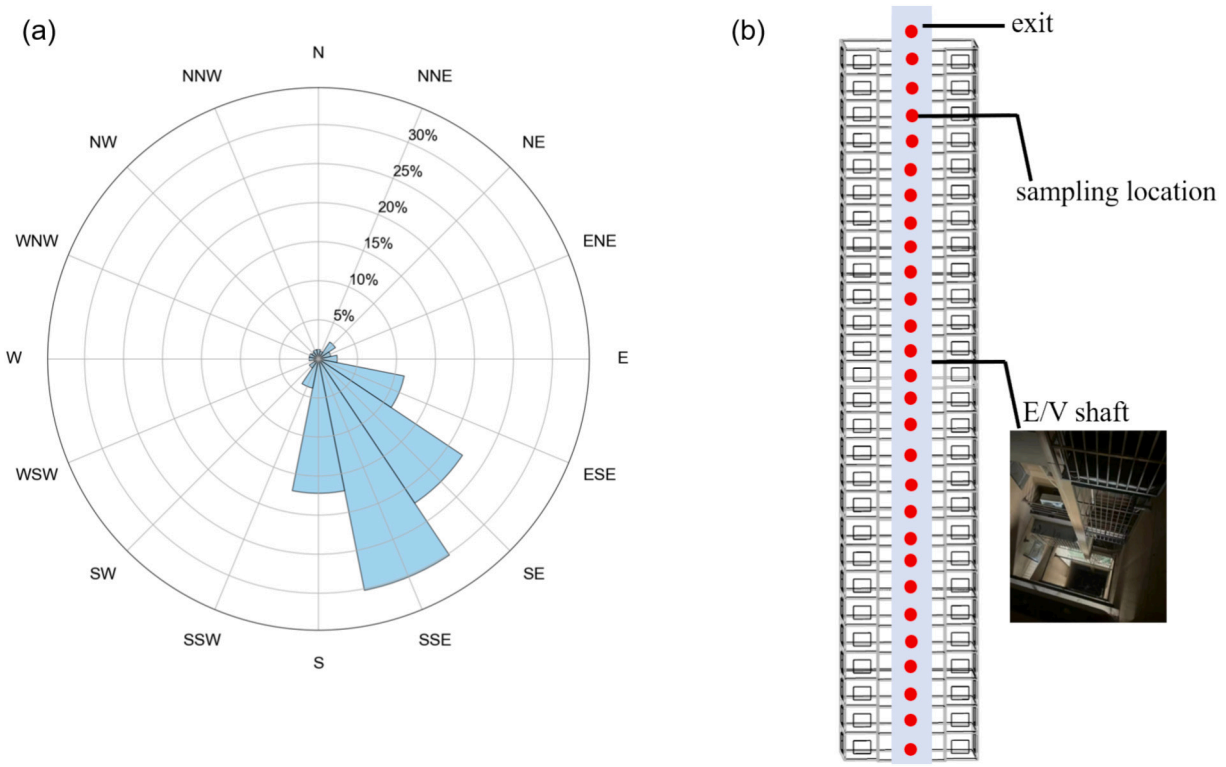

Fig. 5. (a) Wind rose of Nanjing City during May–June 2023; (b) sampling points within the E/V shaft. (For interpretation of the references to color in this figure legend, the reader is referred to the web version of this article.)

frequency data acquisition and logging, ensuring reliable dynamic measurements under typical field conditions such as ambient temperature variations and turbulence.

During sustained southerly wind conditions, when the building was oriented east-west (as shown in Fig. 1, with east-facing and west-facing façades), the southerly wind direction was approximately parallel to the building's main façade, airflow primarily entered through the openings on one side of the façade and exited from the opposite side. Accordingly, the dominant wind velocity along this direction was prescribed in the numerical model as the inflow and outflow boundary conditions. In the observational analysis, time periods consistent with this wind direction were extracted from the long-term dataset for comparison and validation of the simulation results (Fig. 1a). U_z and p data were collected at every floor from F1 to F33. Each sampling point was positioned at least 1.2 m away from the parapet to minimize flow interference from the structure. Over 1000 data points were recorded at each station to ensure statistical robustness.

2.4. Definition of chimney effect index

The dimensionless number Chimney Effect Index (CEI) is defined in this study to measure the strength of vertical airflow inside the E/V shaft and how it is affected by wind velocity building height, and building window opening area.

$$CEI = \ln\left(\frac{(\overline{U_z(z)})^2}{\overline{U_{hor}(z)}} \times \frac{\mathrm{A}}{H}\right) \tag{13}$$

$$\overline{U_{hor}(z)} = (\overline{U_x(z)})^2 + (\overline{U_y(z)})^2 \tag{14}$$

In Eq. (13) $\overline{U_z}$ is the mean value of the vertical wind velocity component at the internal height z of the E/V shaft, A is the total area of window openings on the windward side of the building, and H is the height of the building, and in Eq. (14) $\overline{U_x}$ is the mean value of the wind velocity component in the x-direction at the internal height z of the E/V shaft, and $\overline{U_y}$ is the mean value of the wind velocity component in the y-direction at the internal height z of the E/V shaft. $\overline{U_{hor}(z)}$ denotes the square of the resultant horizontal wind velocity at height z within the E/V shaft.

3. Results and discussion

3.1. Simulation and observation comparison

Fig. 6 presents a comparison between observations and simulations for the A10 scenario. In this scenario, the vertical component of airflow velocity (U_z) and pressure (p) inside the E/V shaft were simulated at multiple floor heights because A10 best represents the building's typical operating state shown in Fig. 1. Observational profiles acquired from the same building were then compared with the simulated results; the comparison is summarized in Fig. 6.

Both observed and simulated fields within the E/V shaft exhibit strong spatial heterogeneity, while the observational data additionally contain temporal variability associated with intermittent turbulence. To facilitate a robust comparison, box-and-whisker plots are used: Fig. 6(a) shows the statistical distribution of wind speed (observation: blue; simulation: red), and Fig. 6(b) shows the statistical distribution of pressure (observation: green; simulation: pink). The pressure plot uses the left ordinate for measured atmospheric pressure P (unit: hPa) and the right ordinate for model-derived relative pressure p. Because p is referenced to the model's zero boundary, it cannot be compared directly with absolute atmospheric pressure in magnitude; nevertheless, variations in p reliably reflect the trend and range of actual pressure changes, and therefore agreement is assessed by comparing trends and ranges between P and p. Horizontal axes denote floor numbers; vertical axes display five summary statistics corresponding to the 95%, 75%, 50% (median), 25% and 5%.

The comparison reveals that both observed and simulated U_z increase with height, peaking near the F30 before gradually weakening at higher elevations. The consistently positive mean values across most sampled levels indicate that updrafts prevail throughout a substantial portion of the shaft. In the model, the kinematic pressure (p) decreases by approximately 15 m^2/s^2 from the lowest to the highest floor. This trend is consistent with the observed static pressure (P), which decreases from approximately 1012.4 hPa to 1012.2 hPa over the same height range. Observed U_z ranges from −0.20 m/s to 3.30 m/s, with the maximum occurring near the F30. In the simulation, the U_z reaches its minimum median value of −0.04 m/s at the F1, indicating a weak downdraft; it attains a maximum of 2.5 m/s at F30, before falling to 0.4 m/s near the shaft exit. The pressures P and p, on the other hand, exhibit an accelerated decrease from the middle to upper levels and attain their minima at the exit.

Overall, the comparison suggests that the intensity and vertical distribution of airflow and pressure within the E/V shaft are closely linked to both the structural configuration of the HRTB and the spatial distribution of the external background wind field. Floor-level airflow results from the interaction between each floor's ventilation characteristics and the external wind-induced flow or pressure; inter-floor heterogeneity further promotes the formation and persistence of vertical flows within the shaft.

In this study, certain discrepancies were observed between the numerical simulations and field measurements. These differences can be attributed to several factors. First, limitations in instrumentation and observational accuracy-including sensor precision and variations in the actual geometry of older, retrofitted atrium spaces-may have introduced deviations. Despite careful alignment of observation sites with the corresponding simulation monitoring points, this issue remains evident in complex vertical environments. Second, simplifications in model parameterization, such as predefined window-opening configurations and assumed background wind conditions, may not fully capture the dynamic and heterogeneous nature of ventilation processes, including inter-floor airflow interactions. During the field campaign, coordination with building management was conducted to maintain ventilation conditions as consistent as possible with the modeling assumptions. However, real-world operational constraints prevented perfect alignment, thereby introducing additional variability. Third, long-term renovations and occupant-driven modifications have resulted in structural heterogeneity, altering the layout and connectivity of ventilation shafts as well as the distribution of openings. These features deviate from the idealized model configuration. Collectively, these factors highlight the inherent challenges in achieving exact agreement between simulations and measurements in complex HRTBs. Nevertheless, the observed discrepancies remain within an acceptable range and do not undermine the main conclusions of this study. This outcome underscores the importance of integrating refined field experiments with model development to improve the representation of real-world ventilation mechanisms.

3.2. CFD results: sensitivity of ventilation area

Figs. 7(a-b) and Figs. 7(e-g) display projected velocity vectors (black arrows) and wind velocity magnitude (color scale) for each floor and the vertical connecting area inside the building under the A10 scenario. Figs. 7(c-d) present the simulated pressure field p; vectors in these panels indicate local flow direction and magnitude. Here, Figs. 7(a-d) show the xOz and yOz longitudinal sections, while Figs. 7(e-g) correspond to the horizontal cross-sections of the F2, F16, and F31, respectively.

When the windward and leeward window openings are both 10 m^2, external flow enters the rooms through the windward windows and generates a complex internal flow field. Part of this incoming flow exits through side (leeward) windows on the same floor, while another portion enters the vertically connected area (E/V shaft) and acquires a significant vertical velocity component (U_z). Overall, the majority of the airflow exits via the leeward windows on the same floor and gradually returns toward the outdoor background wind speed ($U = 5\ m/s$) (Fig. 7).

From Figs. 7(c-d), the modeled pressure p inside the E/V shaft is generally lower than in the horizontal rooms and decreases with elevation; the rate of decrease accelerates above approximately 60 m and attains a minimum in the vicinity of the shaft exit, with an overall decrease of about 15 m^2/s^2. This vertical pressure decline can be attributed to the superposition of two effects: (1) increasing flow speed with height produces local reductions in static pressure through the conversion between kinetic and static pressure (as described by Bernoulli's principle i.e., the conservation of energy along streamlines); and (2) the ambient hydrostatic pressure decreases with elevation according to the hydrostatic relation. The combined action of these mechanisms yields the observed reduction in

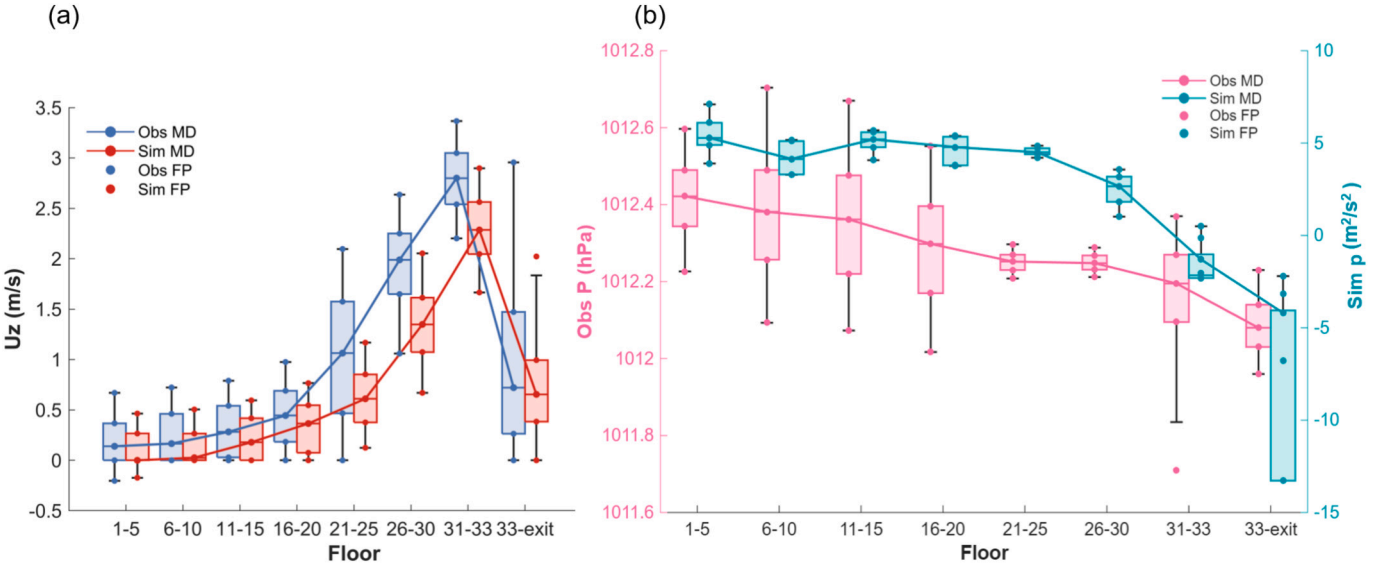

Fig. 6. Comparison between simulation and observation results in the E/V shaft region for A10. (a):simulated $U_z$values (red) and observed results (blue); (b): simulated p values (green) and observed P results (pink), with the left axis showing observed P (hPa) and the right axis presenting simulated p (m^2/s^2); observation median (Obs MD); simulation median (Sim MD); observation feature points (Obs FP); simulation feature points (Sim FP); rooftop exit (exit). (For interpretation of the references to color in this figure legend, the reader is referred to the web version of this article.)

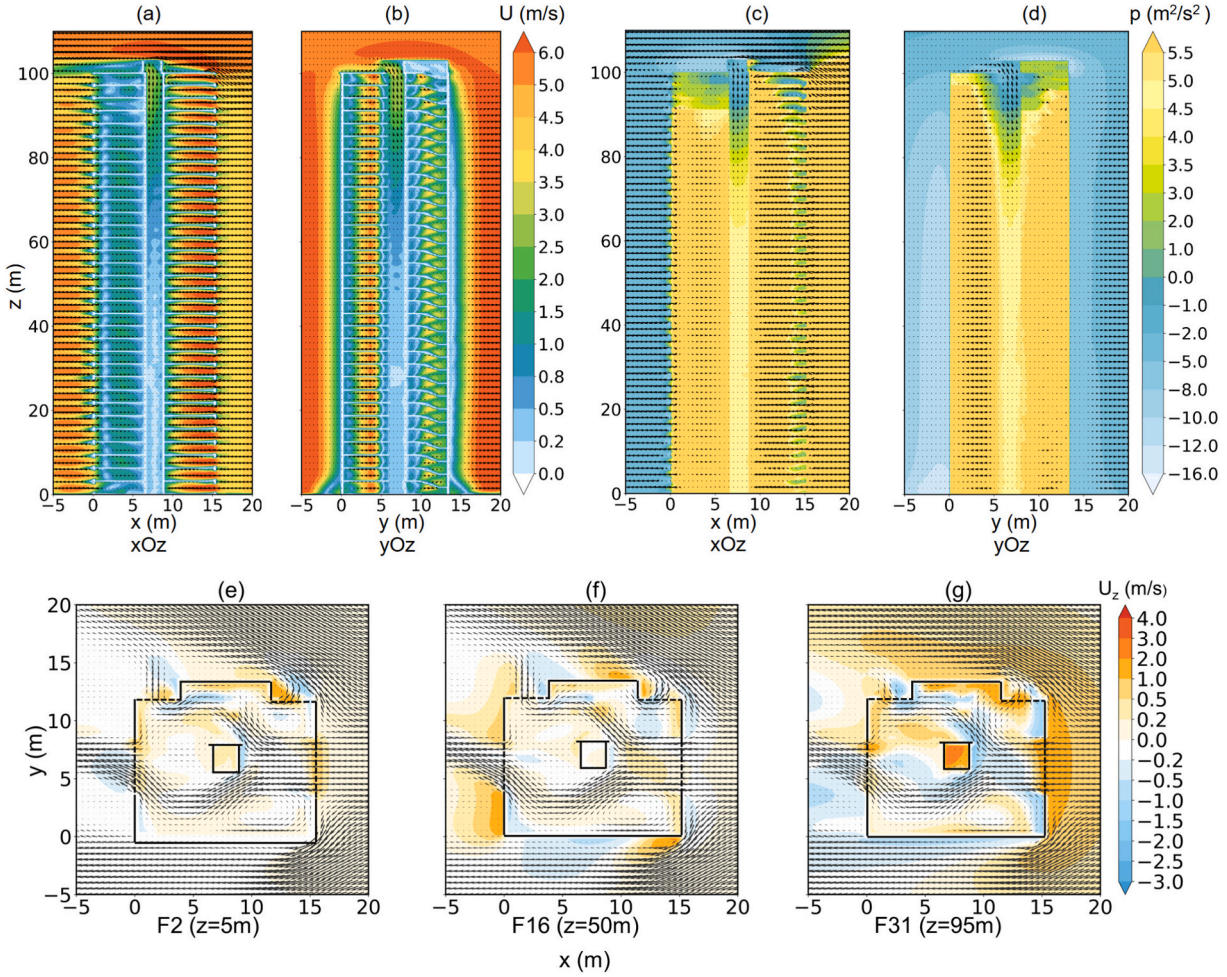

Fig. 7. Simulated wind field and pressure filed for A10, (a): wind field in the *xOz* section; (b): wind field in the *yOz* section, wind velocity magnitude (m/s) shown as a color map, with velocity vectors representing projections on the section; (c): pressure field in the *xOz* section; (d): pressure field in the *yOz* section, *p* distribution shown as a color map, with velocity vectors representing wind projections on the section; F2 (e), F16 (f), and F31 (g): vertical wind velocity (U_z) magnitude distribution at different floors, wind velocity magnitude (m/s) is shown as a color map, with velocity vectors representing the wind projections on the *xOy* sections.

p, which is consistent with the spatial variation of wind speed shown in the velocity fields. (Note that in this model *p* is a relative pressure referenced to the model zero boundary; therefore, comparison with absolute atmospheric pressure is made in terms of trends and ranges rather than absolute magnitudes.)

The basic pattern of the flow field is similar across floors given the same interior layout, with pronounced through-flow ventilation in all representative floors; nevertheless, there are modest differences between floors in the magnitudes of wind speeds and the locations of vortical structures. As the vertically directed flow traverses successive floors, the vertical component within the E/V shaft evolves and ultimately produces a coherent updraft. The updraft velocity increases with floor height: the maximum U_z in this scenario is simulated to be approximately 2.5 m/s around the F31 (Fig. 7(g)), whereas U_z on the lower and middle floors (about the F1-F20) is on the order of 0.2 m/s (Figs. 7(e)–(f)).

Figs. 8(a-b) and Figs. 8(e-g) present the simulation results of the wind field and pressure field in the A16 scenario. The color scale and vector settings are consistent with those used in Fig. 7. In the A16 scenario, the ventilation openings on different floors of the building remain consistent, but the ventilation area is larger (16 m^2 in A16 compared to 10 m^2 in A10).

The spatial distribution of indoor airflow velocities and flow characteristics on different floors in the A16 scenario is generally similar to that of the A10 scenario. However, the average indoor air velocity increases, while the velocity gradient decreases compared to A10. This behavior can be attributed to two combined effects: first, the increase in floor-by-floor ventilation area reduces the resistance of external airflow through each floor, thereby enhancing indoor ventilation; second, the larger ventilation openings weaken the wind pressure gradient between floors, reducing the forcing effect of the pressure gradient that drives the generation and maintenance of U_z in the E/V shaft. As a result, U_z within the E/V shaft in the A16 scenario is overall significantly lower than in A10, particularly around the F31, where it is approximately 40% lower than in the A10 scenario.

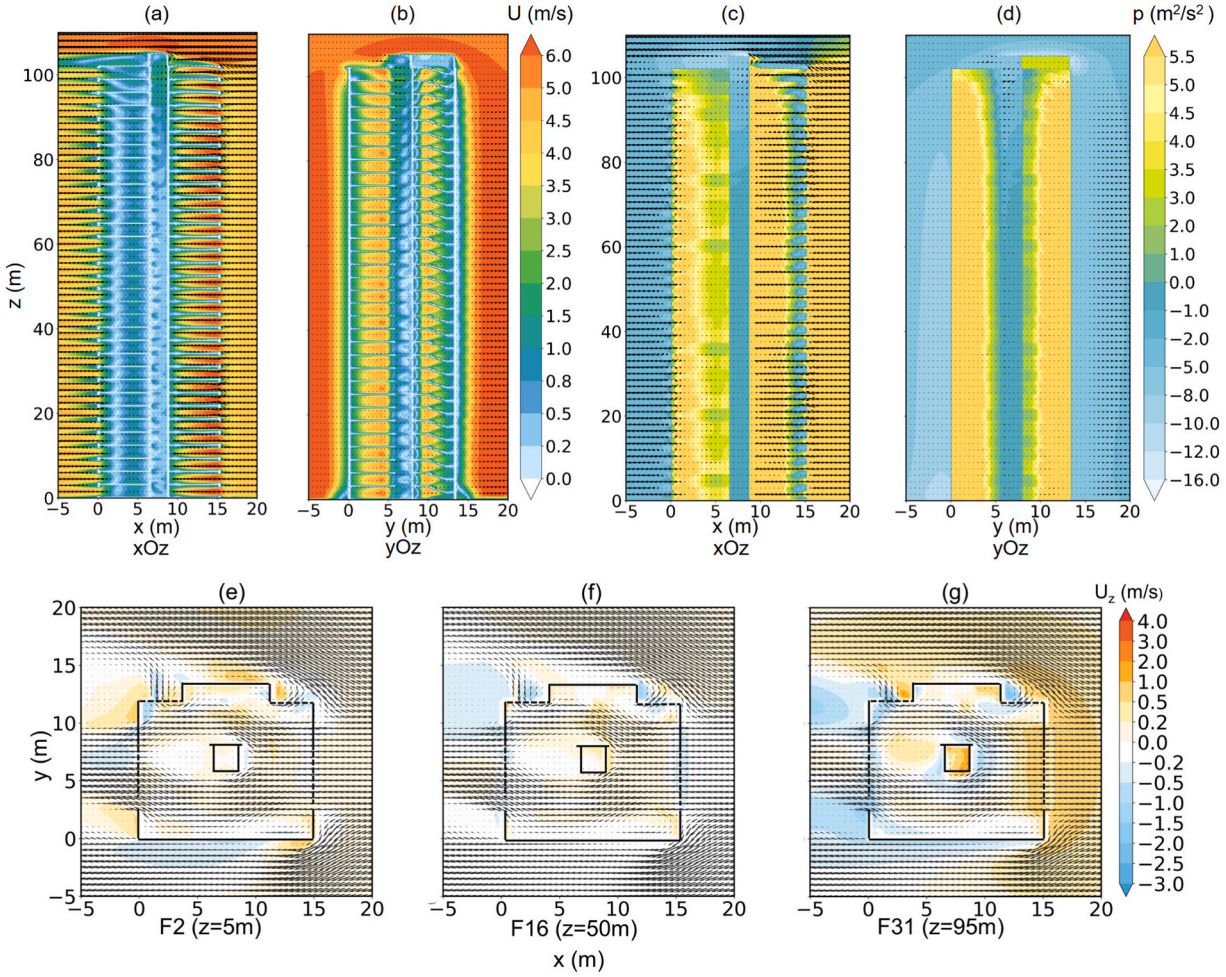

Fig. 8. Simulated wind field and pressure filed for A16, (a): wind field in the *xOz* section; (b): wind field in the *yOz* section, wind velocity magnitude (m/s) shown as a color map, with velocity vectors representing projections on the section; (c): pressure field in the *xOz* section; (d): pressure field in the *yOz* section, *p* distribution shown as a color map, with velocity vectors representing wind projections on the section; F2 (e), F16 (f), and F31 (g): vertical wind velocity (U_z) magnitude distribution at different floors, wind velocity magnitude (m/s) is shown as a color map, with velocity vectors representing the wind projections on the *xOy* sections.

In the A16 scenario, *p* continues to decrease gradually with height. The difference in *p* between the E/V shaft and the horizontal floors becomes larger. Nevertheless, within the vertical distribution of the E/V shaft, the magnitude gradient of *p* is smaller compared to A10, with an overall decrease of about 5 m^2/s^2 from top to bottom. This is because horizontal floor ventilation is substantially improved, which reduces the wind speed gradient within the E/V shaft. Consequently, the pressure difference between the vertical region and the horizontal region at the same height increases, while the variation of *p* along the vertical direction is much smaller.

Furthermore, Figs. 8(e-g) show the horizontal wind speed distributions at 5 m, 50 m, and 95 m above ground level for the lower (F2), middle (F16), and upper (F31) floors in the A16 scenario. The results indicate a significant enhancement of horizontal indoor airflow in A16, with an average increase of 22% in horizontal air velocity compared to A10. This observation is consistent with the analysis presented in Fig. 6.

Figs. 9(a-b) and Figs. 9(e-f) present the simulation results of the wind field and pressure field in the L10 scenario. In this scenario, the lower floors (F1-F11) are well ventilated, with 10 m^2 windows on both the windward and leeward sides, while the middle and upper floors (F12-F33) have no ventilation openings. While the middle and upper floors (F12-F33) have no ventilation openings on either side.

From Figs. 9(a-b), it can be observed that within the F1-F11, *U* on each floor is generally similar to that in the corresponding floors of the other scenarios, whereas above the F12, the wind speed decreases significantly. Simultaneously, the spatial distribution of both the wind velocity and pressure fields in the vertical connectivity region (E/V shaft) exhibits pronounced changes. Specifically, *U* in the E/V shaft at the center of the middle and upper floors (Fig. 9(f)) is substantially stronger than that in the lower floors (Fig. 9(e)), with *U* in the middle floors reaching up to 6 m/s—approximately 95% higher than in the lower floors. The kinematic pressure (*p*) in the E/V shaft is generally lower than that in the horizontal rooms, and it decreases gradually with height. On the lower floors and in regions

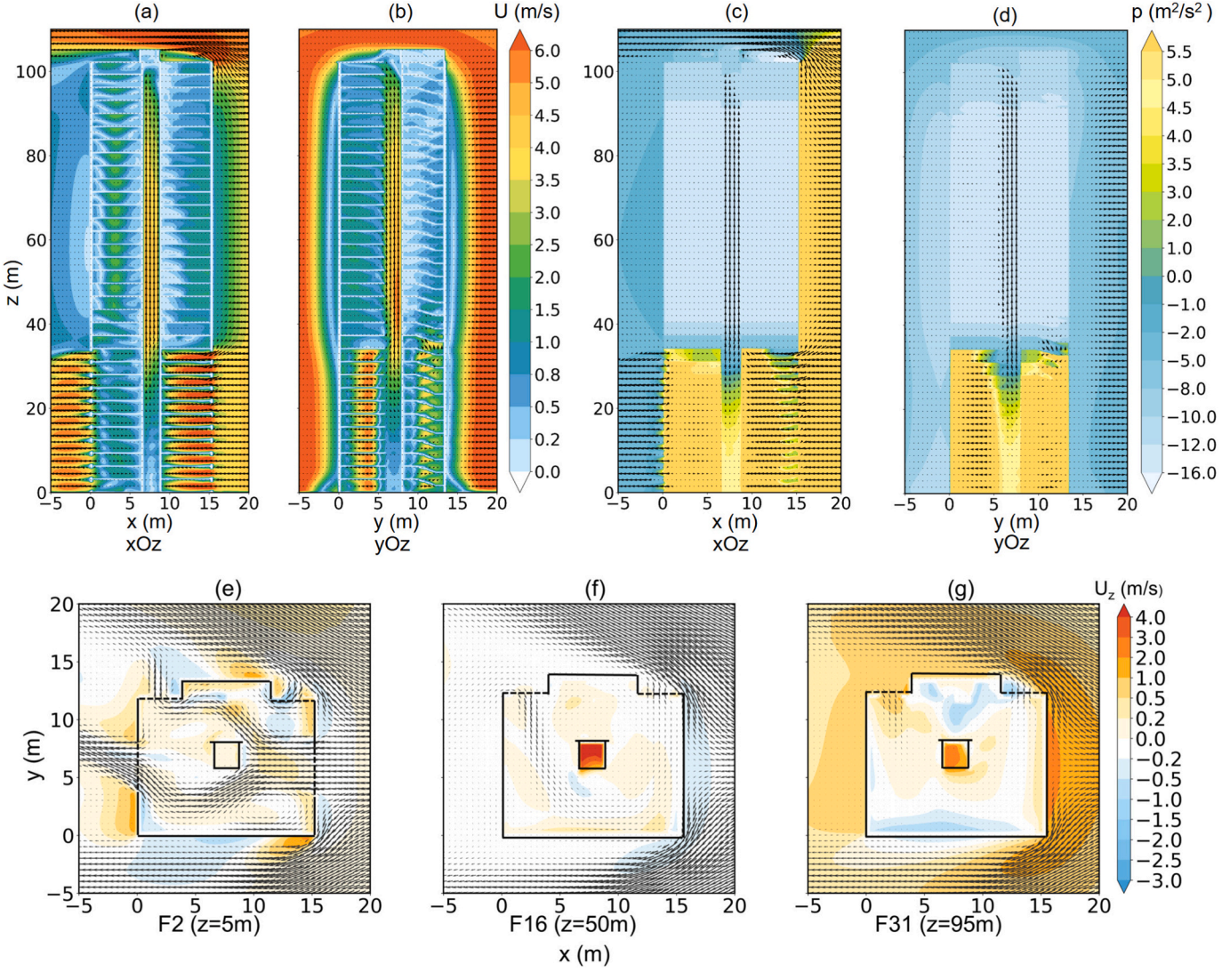

Fig. 9. Simulated wind field and pressure filed for L10, (a): wind field in the *xOz* section; (b): wind field in the *yOz* section, wind velocity magnitude (m/s) shown as a color map, with velocity vectors representing projections on the section; (c): pressure field in the *xOz* section; (d): pressure field in the *yOz* section, p distribution shown as a color map, with velocity vectors representing wind projections on the section; F2 (e), F16 (f), and F31 (g): vertical wind velocity (U_z) magnitude distribution at different floors, wind velocity magnitude (m/s) is shown as a color map, with velocity vectors representing the wind projections on the *xOy* sections.

where ventilation changes markedly, p decreases sharply, corresponding to regions of rapid wind speed variation. From the middle to the upper floors, the kinematic pressure (p) gradually decreases, reaching a minimum near F20 before slightly increasing toward the top. Overall, p varies by approximately 20 m^2/s^2 within the E/V shaft, with a net reduction of about 5 m^2/s^2 from the bottom to the exit.

On the upper floors (Fig. 9(g)), under the influence of the obstruction from the top floor, the airflow gradually changes direction, and its vertical component becomes relatively weaker. The L10 scenario intensifies the central E/V shaft updraft significantly, yielding a maximum U_z of 4 m/s at F20—notably higher than the ~2.5 m/s in A10 and ~ 1.5 m/s in A16, representing increases of ~60% and ~160%, respectively. The rate of change of U_z along the vertical direction is highest in the L10 scenario.

By comparing the simulation results of the A10, A16, and L10 scenarios and integrating observational data, it is evident that a non-zero U_z commonly exists in the E/V shaft region of HRTBs, representing the so-called chimney effect. The primary mechanism underlying this phenomenon is the inter-story variation in airflow resistance caused by differences in external background wind speed, spatial layout, and ventilation area across floors. This inter-story difference induces a stack-induced pressure gradient along the vertical direction in the E/V shaft, which in turn drives the vertical airflow component. The higher inter-story ventilation resistance in the middle and upper floors in L10 further strengthens the vertical pressure gradient, resulting in both enhanced U_z and more pronounced variations in p along the vertical direction.

Comparative analysis between A10 and A16 scenarios indicates that higher intra-story ventilation efficiency reduces the stack-induced pressure gradient and vertical wind velocity within the E/V shaft. In contrast, the L10 scenario shows a pronounced increase in the inter-story ventilation resistance gradient. The average U_z in L10 is approximately 50% higher than in A10 and 70% higher than in A16, where more floors are ventilated. Additionally, the U_z-height (z) contour within the E/V shaft is most prominent

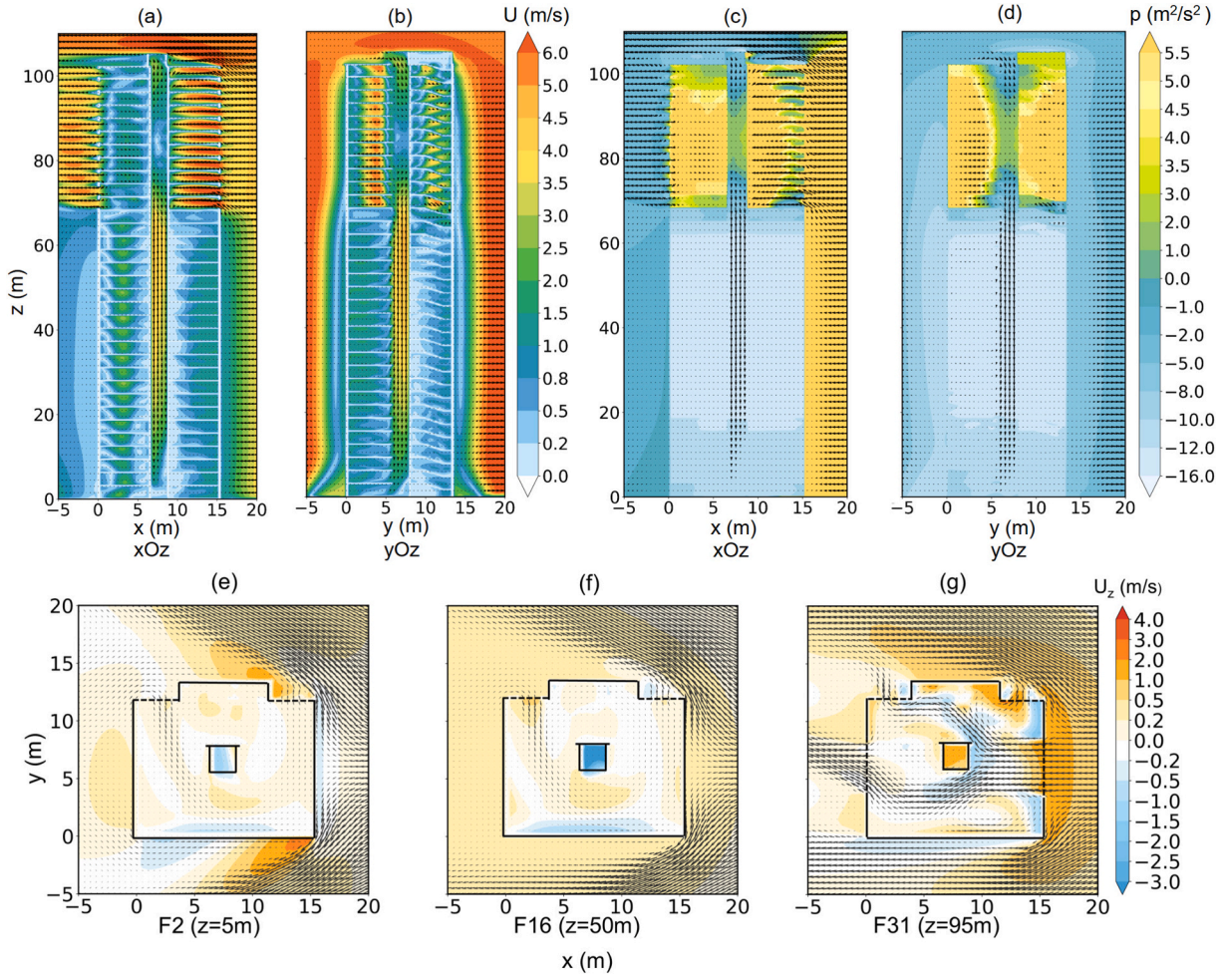

Fig. 10. Simulated wind field and pressure filed for UP10, (a): wind field in the *xOz* section; (b): wind field in the *yOz* section, wind velocity magnitude (m/s) shown as a color map, with velocity vectors representing projections on the section; (c): pressure field in the *xOz* section; (d): pressure field in the *yOz* section, p distribution shown as a color map, with velocity vectors representing wind projections on the section; F2 (e), F16 (f), and F31 (g): vertical wind velocity (U_z) magnitude distribution at different floors, wind velocity magnitude (m/s) is shown as a color map, with velocity vectors representing the wind projections on the *xOy* sections.

and intense in the L10 scenario. This suggests that larger ventilation resistance in the middle and upper floors, superimposed on strong lower-floor ventilation, promotes a stronger chimney effect. It can be further inferred that taller HRTBs are more likely to exhibit a pronounced chimney effect, as the inter-story ventilation resistance gradient is generally larger in taller buildings, and the vertical gradient of external horizontal wind speed between the top and lower levels is inherently greater, which favors the generation and maintenance of a stack-induced pressure gradient within the E/V shaft.

Moreover, the L10 scenario bears resemblance to the condition during a fire in the lower floors of an HRTB: a large ventilation area forms on the lower floors due to window failure, while occupants may close windows on middle and upper floors for safety, reducing ventilation in these regions. According to the L10 simulation results, such a configuration further enhances the vertical suction effect of the E/V shaft, generating a stronger updraft. This mechanism may help explain the phenomenon observed in Fig. 1, where embers transported by an intensified U_z ascend the E/V shaft, potentially igniting items on middle floors and causing secondary fires that bypass lower floors.

Figs. 10(a-b) and Figs. 10(e-f) show the wind simulation results for the UP10 scenario. As illustrated in Fig. 10, no airflow enters the interior of the building through openings on the windward side of the lower and middle floors (F1-F22, no windward or leeward openings), whereas the windward vents on the upper floors (F23-F33, 10 m^2 openings) introduce external airflow into the interior. Some of this airflow passes directly through the interior rooms and exits via the leeward windows, while a portion is transported downward through the centrally located E/V shaft. Consequently, indoor velocities in the lower and middle floors remain low, ranging from approximately 0 to 1.5 m/s, dominated by the downward transport from the upper floors, whereas the indoor air velocities in the upper floors are higher, ranging from about 1.5 to 3 m/s.

From the Fig. 10(f), a pronounced downward airflow is observed in the E/V shaft in the middle and lower floor regions, with U_z reaching approximately 4.5 m/s, likely due to the inertia of the descending flow originating from the upper floors. Conversely, upward airflow occurs in the upper-floor region of the E/V shaft (around F30-F33), with U_z reaching about 1.5 m/s (Fig. 10(g)), which may be enhanced by the suction effect at the rooftop exit, where U_z reaches about 2.5 m/s.

Regarding pressure, the simulated p (in m^2/s^2) in the middle and lower floors decreases by approximately 5 m^2/s^2 overall. Around 80 m height, p sharply increases by roughly 15 m^2/s^2 due to the presence of a small region with very low wind velocity. With increasing floor height and improved ventilation conditions on the upper floors, p gradually decreases again by about 5 m^2/s^2 toward the exit. The variation of p in m^2/s^2 reflects the combined effects of vertical airflow transport, local velocity deficits, and inter-floor ventilation conditions within the E/V shaft.

Based on the simulation results of the four scenarios A10, A16, L10 and UP10, we hypothesize that the difference in airflow resistance between the floors of the building creates a vertical wind pressure gradient within the E/V shaft, which is the main driver of the chimney effect in this area. With the same ventilation area at each floor, the results of A10 vs. A16 show that a larger ventilation area reduces the wind pressure gradient and hence the chimney effect. A plausible conclusion is that when the ventilation area at each floor is maximized (e.g., completely open, removing all building components that contribute to the background wind field), U_z will tend to zero. In the case of unequal ventilation areas, the larger ventilation area at the lower floors in the L10 scenario favors airflow ingress into the E/V shaft, while horizontal ventilation is almost absent on the middle and upper floors. In addition, the connectivity of the rooftop to the outside background wind field (background wind speeds are higher than ground level wind speeds) together

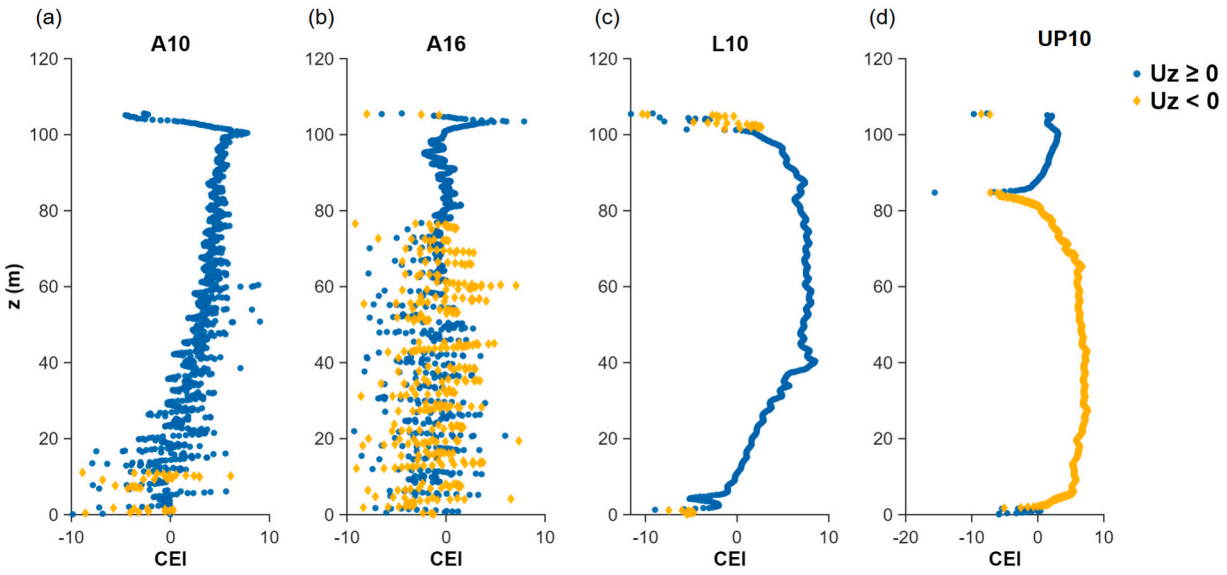

Fig. 11. Vertical profiles of simulated CEI for four scenarios (A10, A16, L10, UP10), the orange diamonds represent the CEI when $U_z < 0$, and the blue dots represent the CEI values when $U_z \geq 0$, (a-d) illustrate the variation of CEI with z (height) for four scenarios (A10, A16, L10, UP10). (For interpretation of the references to color in this figure legend, the reader is referred to the web version of this article.)

contributes to more favorable airflow discharge conditions within the E/V shaft, resulting in the strongest upward U_z profile, i.e., the most significant chimney effect, in this scenario. In contrast, the stack wind pressure gradient between the horizontal ventilation set up at the upper floors and the vents at the top of the E/V shaft is weaker in the UP10 scenario than in the L10 scenario, and fails to effectively create a suction effect on the lower and middle floors. At the same time, the absence of ventilation window openings on the lower and middle floors leads to a reversal of the vertical wind pressure gradient, generating a downward U_z, which is lower in magnitude compared to that in A10 and L10.

3.3. Comparative analysis of vertical profiles of CEI in four scenarios

Fig. 11 shows the simulation results of the vertical profile of CEI further derived from the vertical distribution of U_z obtained in the four simulation scenarios. The horizontal coordinate represents the values of the CEI, a dimensionless number. The vertical coordinate represents height. The reported U_z values are confined to the E/V shaft region of the HRTB. In the Fig. 11, negative U_z values are indicated by orange diamonds, whereas non-negative U_z values are indicated by blue dots.

As shown in the Fig. 11, the CEI vertical profiles of A10 and L10 scenarios are dominated by blue color, indicating that the U_z in the E/V shaft region is mainly upwelling. In particular, the CEI values for L10 are higher, with a stronger peak intensity and a wider vertical range, showing a stronger and more pronounced chimney effect. In contrast, the CEI profile of A16 is similar to that of A10, but the overall values are significantly weaker with more orange diamonds appearing, indicating a weakening of the updraft trend, while the trend of the CEI profile of UP10 is significantly different from that of the other three scenarios, with the orange diamonds dominating at all altitude levels, indicating a predominantly subsiding flow in the E/V shaft in UP10 scenario. Suggesting that the airflow in the E/V shaft in this scenario is mainly sinking. Moreover, as indicated by the blue and orange markers, when $U_z \geq 0$, larger CEI values correspond to stronger upward airflow, reflecting a more intense wind-driven chimney effect in the E/V shaft.

Fig. 12(a) shows the variation of U_z within the E/V shaft under the four scenarios, while Fig. 12(b) shows the simulated distribution of p within the same region. The comparison of these four scenarios indicates that inter-floor differences in cross ventilation, determined by the window opening area on each floor, play a pivotal role in shaping the vertical airflow within the E/V shaft. Additionally, the logarithmic vertical distribution of background atmospheric wind velocity which generally increases with height, results in horizontal wind speeds at the rooftop being substantially higher than those near ground level, thereby providing an additional driving force for the formation of upward airflow in the E/V shaft. This mechanism can also be interpreted through the Bernoulli equation.

Furthermore, as the building height increases, the pressure differences between upper and lower floors tend to become more pronounced, which further reinforces the vertical driving force and enhances U_z, contributing to the intensification of the chimney effect as defined in this study. Importantly, this effect can be mitigated by enhancing cross-floor ventilation, i.e., by increasing the ventilation area and reducing intra-story airflow resistance. These findings provide valuable insights for the detailed investigation of building ventilation efficiency and the potential transport characteristics of indoor pollutants.

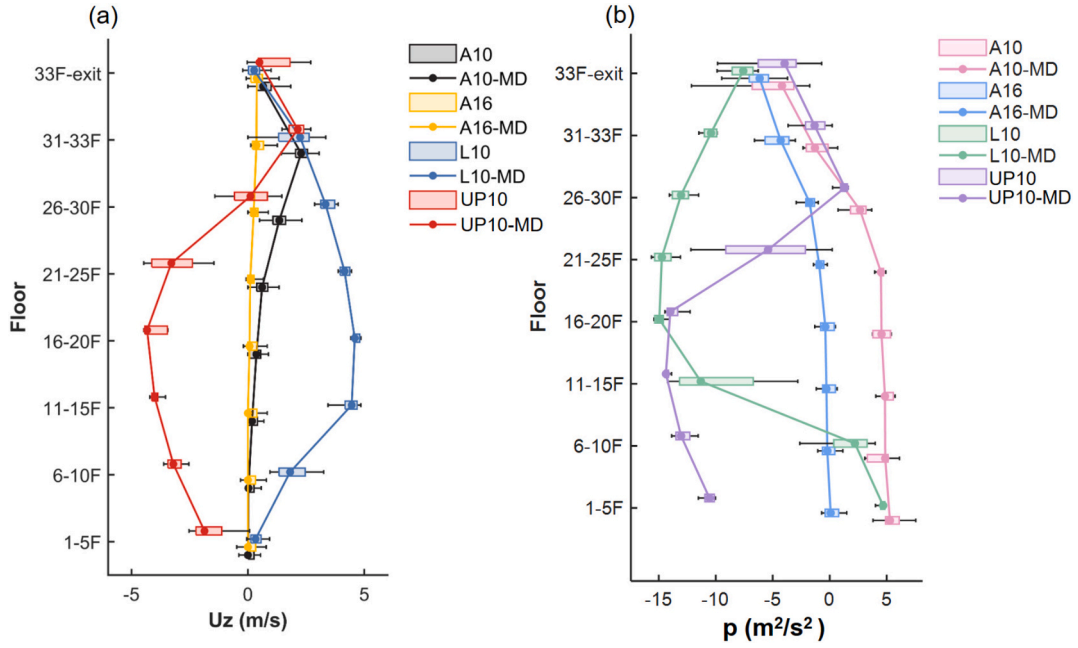

Fig. 12. Box plot of U_z and p inside the E/V shaft for four scenarios (A10, A16, L10, UP10), (a): box plot of U_z; (b): box plot of p; rooftop exit (exit); median (MD); vertical wind velocity component (U_z); pressure (p).

4. Conclusion

In this study, a high-resolution CFD model was employed to simulate three-dimensional wind and pressure fields under cross-ventilation conditions, both inside and outside a representative HRTB, focusing on how the internal spatial configuration—particularly the vertical E/V shaft and floor-level ventilation layout—modulates the indoor airflow dynamics. Field observations were used to validate the simulated vertical profiles of the vertical wind component (U_z) and kinematic pressure (p) within the E/V shaft. Additional parametric simulations were conducted to examine how variations in horizontal ventilation areas across different floors influence the U_z within the E/V shaft and the overall indoor flow structure. The results elucidate the mechanisms governing the formation and enhancement of the wind-driven chimney effect within HRTBs, which directly arise from the building's internal spatial configuration. Notably, the chimney effect identified herein is purely wind-induced, highlighting the decisive role of internal spatial configuration and ventilation layout in generating vertical airflow, independent of thermal buoyancy. The main findings are summarized as follows:

1. HRTBs are typically designed with vertically connected structural regions. Under a given background wind field, a gradual increase in U_z with height is observed inside the E/V shaft. This trend is consistent with field measurement data. Critically, this wind-driven upward flow occurs even in the absence of thermal buoyancy, highlighting that the internal architectural layout itself is a primary driver of the flow regime.

2. Altering the window-opening area across floors markedly affects indoor airflow characteristics, especially the vertical updraft within the E/V shaft. Increasing the horizontal ventilation area by 60% (from 10 m^2 to 16 m^2) enhances horizontal wind speed on each floor by approximately 22%. However, this strengthened cross-ventilation simultaneously reduces the inter-floor pressure difference, resulting in an estimated 40% decrease in vertical velocity (U_z) within the E/V shaft. When large ventilation openings are provided only on the lower floors (F1-F11), while the middle and upper floors (F12-F33) remain sealed, a strong upward airflow develops inside the shaft. This configuration, represented by the L10 scenario in the present study, characterizes the so-called chimney effect. The averaged U_z in L10 increases by about 50% compared to the A10 scenario, where all floors share identical ventilation openings. These findings suggest that the wind-driven chimney effect could be a key mechanism driving the rapid upward spread of fire in HRTBs when ignition occurs at lower levels.

3. Both observations and simulations demonstrate that the vertical airflow in the E/V shaft is predominantly controlled by inter-floor ventilation, which redistributes the vertical pressure. High roof-level wind speeds create a low-pressure region at the E/V shaft top, inducing upward airflow. Enhanced ventilation at lower floors increases the top-bottom pressure gradient or reduces inlet resistance, thereby strengthening vertical motion. In contrast, intensified upper-floor ventilation can generate reverse downward flow toward the lower floors. This pressure profile generally decreases along the building height with increasing wind speed, whereas abrupt increases occur near openings in transition zones. The resulting pressure differences promote upward discharge through the shaft outlet. This establishes a direct causal link between the internal spatial pattern (ventilation opening distribution) and the resulting indoor transport phenomena.

4. This study bridges the gap between atmospheric transport principles and indoor airflow dynamics by demonstrating how internal building geometry governs flow patterns. The results highlight that vertical airflow can arise solely from building geometry, emphasizing the need to mitigate uncontrolled upward transport in vertical shafts through measures such as shaft compartmentalization and isolating fire-prone areas like kitchens. Controlled lower-level ventilation can promote beneficial vertical exchange while minimizing pollutant accumulation. Although fire scenarios were not explicitly simulated, the identified wind-driven chimney effect indicates that vertical shafts could intensify smoke rise under fire conditions. These findings underscore that internal spatial design is as critical as external form in predicting and managing atmospheric transport within urban buildings, offering a new perspective for environmental modeling and sustainable building design in high-density cities.

5. Limitations and barriers of research

This study has several limitations that should be acknowledged. First, although the simulations demonstrate that building geometry alone can induce vertical airflow in tower structures, the combined influence of structural and thermal drivers was not quantified due to the absence of thermo-fluid coupling. It should be noted that the current model deliberately isolates wind-driven vertical airflow, excluding thermal buoyancy, in order to specifically investigate the purely wind-induced chimney effect. While this simplification is theoretically justified, it constrains the applicability of the results to scenarios where thermal gradients play a significant role. Second, the analysis was conducted under meteorological conditions specific to Nanjing, and therefore the findings may not be generalizable to other climatic regimes, where airflow and pollutant transport dynamics could differ significantly. Third, the focus on an isolated tower did not account for aerodynamic interactions within dense building clusters, where neighboring structures can significantly modulate vertical air exchange. This study therefore adopts a single-building framework to isolate fundamental airflow mechanisms, while the extension to realistic building clusters is planned as an important direction of future research.

Future research should expand the scope of climatic scenarios, incorporate thermo-fluid coupling, and assess tower performance within realistic urban clusters. These efforts will provide a more comprehensive understanding of airflow mechanisms in high-rise environments and enhance the reliability of model predictions for ventilation and air quality management.

Supplementary data to this article can be found online at https://doi.org/10.1016/j.uclim.2026.102858.

CRediT authorship contribution statement

Junrui Mi: Writing – original draft, Visualization, Validation, Software, Investigation, Data curation. **Zhenxin Liu:** Writing – review & editing, Supervision, Project administration, Methodology, Funding acquisition, Formal analysis, Conceptualization. **Chao Zhang:** Data curation. **Wenqing Shi:** Writing – review & editing. **Yuanyuan Zhang:** Validation. **Hong Liao:** Project administration, Funding acquisition.

Declaration of competing interest

The authors declare that they have no known competing financial interests or personal relationships that could have appeared to influence the work reported in this paper.

Acknowledgments

This work was supported by the Jiangsu Provincial Basic Research Program (Natural Science Foundation) – Carbon Peak and Carbon Neutrality Science and Technology Innovation Special Fund (Frontier and Basic) (Grant No. BK20220031): Coordinated Control of Air Pollution and Climate Under the Context of Carbon Neutrality.

We acknowledge the High-Performance Computing Centre of Nanjing University of Information Science and Technology for their support of this work.

Data availability

The data used in this study, partially used for OpenFOAM simulations and generating relevant figures in the paper, are available at https://doi.org/10.5281/zenodo.18289326.

References

Abd Razak, A., Hagishima, A., Ikegaya, N., Tanimoto, J., 2013. Analysis of airflow over building arrays for assessment of urban wind environment. Build. Environ. 59, 56–65. https://doi.org/10.1016/j.buildenv.2012.08.007.

Adelia, A., Yuan, C., Liu, L., Shan, R., 2019. Effects of urban morphology on anthropogenic heat dispersion in tropical high-density residential areas. Energ. Buildings 186, 368–383. https://doi.org/10.1016/j.enbuild.2019.01.026.

Allegrini, J., 2018. A wind tunnel study on three-dimensional buoyant flows in street canyons with different roof shapes and building lengths. Build. Environ. 143, 71–88. https://doi.org/10.1016/j.buildenv.2018.06.056.

Allegrini, J., Carmeliet, J., 2017. Coupled CFD and building energy simulations for studying the impacts of building height topology and buoyancy on local urban microclimates. Urban Clim. 21, 278–305. https://doi.org/10.1016/j.uclim.2017.07.005.

Antoniou, N., Montazeri, H., Wigo, H., Neophytou, M.K.-A., Blocken, B., Sandberg, M., 2017. CFD and wind-tunnel analysis of outdoor ventilation in a real compact heterogeneous urban area: evaluation using "air delay". Build. Environ. 126, 355–372. https://doi.org/10.1016/j.buildenv.2017.10.013.

Arpino, F., Cortellessa, G., D'Alicandro, A.C., Grossi, G., Massarotti, N., Mauro, A., 2023. CFD analysis of the air supply rate influence on the aerosol dispersion in a university lecture room. Build. Environ. 235, 110257. https://doi.org/10.1016/j.buildenv.2023.110257.

Chen, T., Feng, Z., Cao, S.-J., 2020. The effect of vent inlet aspect ratio and its location on ventilation efficiency. Indoor Built Environ. 29 (2), 180–195. https://doi.org/10.1177/1420326X19865930.

Chen, G., Hang, J., Chen, L., Lin, Y., 2023. Comparison of uniform and non-uniform surface heating effects on in-canyon airflow and ventilation by CFD simulations and scaled outdoor experiments. Build. Environ. 244, 110744. https://doi.org/10.1016/j.buildenv.2023.110744.

Cheung, J.O., Liu, C.-H., 2011. CFD simulations of natural ventilation behaviour in high-rise buildings in regular and staggered arrangements at various spacings. Energ. Buildings 43 (5), 1149–1158. https://doi.org/10.1016/j.enbuild.2010.11.024.

Cui, P.-Y., Zhang, Y., Chen, W.-Q., Zhang, J.-H., Luo, Y., Huang, Y.-D., 2021. Wind-tunnel studies on the characteristics of indoor/outdoor airflow and pollutant exchange in a building cluster. J. Wind Eng. Ind. Aerodyn. 214, 104645. https://doi.org/10.1016/j.jweia.2021.104645.

Deng, J.-Y., Xia, Y., Lao, H., Ye, Y., Wang, Z., Jiang, H., 2024. Natural ventilation potential of teaching building complexes with different block shapes and layout patterns. J. Build. Eng. 96, 110420. https://doi.org/10.1016/j.jobe.2024.110420.

Fallahpour, M., Naeini, H.G., Mirzaei, P.A., 2024. Generic geometrical parametric study of wind-driven natural ventilation to improve indoor air quality and air exchange in offices. J. Build. Eng. 84, 108528. https://doi.org/10.1016/j.jobe.2024.108528.

Fang, Y., Gu, K., Qian, Z., Sun, Z., Wang, Y., Wang, A., 2021. Performance evaluation on multi-scenario urban ventilation corridors based on least cost path. J. Urban Manag. 10 (1), 3–15. https://doi.org/10.1016/j.jum.2020.06.006.

Fini, A.S., Moosavi, A.J.E., Buildings., 2016. Effects of "wall angularity of atrium" on "buildings natural ventilation and thermal performance" and CFD model. Energ. Buildings 121, 265–283. https://doi.org/10.1016/j.enbuild.2015.12.054.

Fu, N., Kim, M.K., Chen, B., Sharples, S., 2022. Investigation of outdoor air pollutant, PM2. 5 affecting the indoor air quality in a high-rise building. Indoor Built Environ. 31 (4), 895–912. https://doi.org/10.1177/1420326X211038279.

Fu, X., Tai, V.C., Moey, L.K., Abd Rahman, N.F., Ahmad, K.A., Baglee, D.J.B., et al., 2024. Opening configurations and natural cross ventilation performance in a double-loaded multi-level apartment building: A CFD analysis. Build. Environ. 254, 111404. https://doi.org/10.1016/j.buildenv.2024.111404.

Gao, C., Lee, W.L.J.B., environment, 2011. Evaluating the influence of openings configuration on natural ventilation performance of residential units in Hong Kong. Build. Environ. 46 (4), 961–969. https://doi.org/10.1016/j.buildenv.2010.10.029.

Gao, Z., Bresson, R., Qu, Y., Milliez, M., De Munck, C., Carissimo, B., 2018. High resolution unsteady RANS simulation of wind, thermal effects and pollution dispersion for studying urban renewal scenarios in a neighborhood of Toulouse. Urban Clim. 23, 114–130. https://doi.org/10.1016/j.uclim.2016.11.002.

Guo, B., Li, L., Zhu, X., Wang, Z., Chen, M., Pei, L., et al., 2025. Identifying the effect of architecture morphology on wind fields and PM2. 5 dispersion at the urban block scale via a combined scheme. Urban Clim. 61, 102443. https://doi.org/10.1016/j.uclim.2025.102443.

Han, X., Li, W., Zhao, Y., Zhuang, Y., Jia, Q., Guan, H., et al., 2024. Organophosphate esters in building materials from China: levels, sources, emissions, and preliminary assessment of human exposure. Environ. Sci. Technol. 58 (5), 2434–2445. https://doi.org/10.1021/acs.est.3c08432.

Hang, J., Yang, X., Ou, C.-Y., Luo, Z.-W., Fan, X.-D., Zhang, X.-L., et al., 2023. Assessment of exhaled pathogenic droplet dispersion and indoor-outdoor exposure risk in urban street with naturally-ventilated buildings. Build. Environ. 234, 110122. https://doi.org/10.1016/j.buildenv.2023.110122.

Hsieh, C.-M., Huang, H.-C., 2016. Mitigating urban heat islands: a method to identify potential wind corridor for cooling and ventilation. Comput. Environ. Urban. Syst. 57, 130–143. https://doi.org/10.1016/j.compenvurbsys.2016.02.005.

Hu, H., Kikumoto, H., Ooka, R.J.J., 2024. Effect of wind direction on natural ventilation in a multiple-room house via field measurements and numerical simulations. J. Wind Eng. Ind. Aerodyn. 248, 105718. https://doi.org/10.1016/j.jweia.2024.105718.
Huang, M., Lau, I., Chan, C.M., Kwok, K.C., Li, G., 2011. A hybrid RANS and kinematic simulation of wind load effects on full-scale tall buildings. J. Wind Eng. Ind. Aerodyn. 99 (11), 1126–1138. https://doi.org/10.1016/j.jweia.2011.09.003.
Huang, Y., Zhou, X., Cao, B., Yang, L., 2019. Effects of ventilation state of vertical shaft on fire tilt direction and smoke migration behaviours in a multi-storey building. Indoor Built Environ. 28 (6), 790–805. https://doi.org/10.1177/1420326X18794767.
Huang, W., Xu, Q., Zhao, B., Lv, Q., Wang, G.J., 2025. Urban multi-scale building energy modeling (BEM) and computational fluid dynamics (CFD) integration: Tools, strategies and accuracy for energy microclimate analysis. J. Build. Eng., 112041 https://doi.org/10.1016/j.jobe.2025.112041.
Jia, L.-R., Han, J., Chen, X., Li, Q.-Y., Lee, C.-C., Fung, Y.-H., 2021. Interaction between thermal comfort, indoor air quality and ventilation energy consumption of educational buildings: a comprehensive review. Buildings 11 (12), 591. https://doi.org/10.3390/buildings11120591.
Jian, Y., Shao, X., Gai, X., Liu, S., Chen, C., Liu, S., 2024. Multizone representation of time-varying airflows in naturally ventilated dwellings: occupant-generated CO2 approach. Energ. Buildings 308, 114038. https://doi.org/10.1016/j.enbuild.2024.114038.
Jiang, Z., Kobayashi, T., Sandberg, M., Yamanaka, T., Kobayashi, N., Choi, N., et al., 2023. Analysis of single-sided ventilation flows of a generic isolated building using particle tracking method in LES simulation. Build. Environ. 235, 110230. https://doi.org/10.1016/j.buildenv.2023.110230.
Jing, Y., Zhong, H.-Y., Wang, W.-W., He, Y., Zhao, F.-Y., Li, Y., 2021. Quantitative city ventilation evaluation for urban canopy under heat island circulation without geostrophic winds: multi-scale CFD model and parametric investigations. Build. Environ. 196, 107793. https://doi.org/10.1016/j.buildenv.2021.107793.
Jo, W.-K., Lee, J.-Y., 2006. Indoor and outdoor levels of respirable particulates (PM10) and carbon monoxide (CO) in high-rise apartment buildings. Atmos. Environ. 40 (32), 6067–6076. https://doi.org/10.1016/j.atmosenv.2006.05.037.
Kahsay, M.T., Bitsuamlak, G.T., Tariku, F., 2019. CFD simulation of external CHTC on a high-rise building with and without façade appurtenances. Build. Environ. 165, 106350. https://doi.org/10.1016/j.buildenv.2019.106350.
Kastner, P., Dogan, T., 2023. A GAN-based surrogate model for instantaneous urban wind flow prediction. Build. Environ. 242, 110384. https://doi.org/10.1016/j.buildenv.2023.110384.
Li, W., He, Y., Zhang, Y., Su, J., Chen, C., Yu, C.W., et al., 2019. LES simulation of flow field and pollutant dispersion in a street canyon under time-varying inflows with TimeVarying-SIMPLE approach. Build. Environ. 157, 185–196. https://doi.org/10.1016/j.buildenv.2019.04.049.
Lin, P., Qin, H., Lau, S.S.Y., Wei, Q.J.B., Environment., 2025. Impact of unit type and configuration on indoor natural ventilation performance of high-rise, high-density residential buildings in Hong Kong. Build. Environ. 269, 112444. https://doi.org/10.1016/j.buildenv.2024.112444.
Liu, P.-C., Lin, H.-T., Chou, J.-H.J.B., Environment., 2009. Evaluation of buoyancy-driven ventilation in atrium buildings using computational fluid dynamics and reduced-scale air model. Build. Environ. 44 (9), 1970–1979. https://doi.org/10.1016/j.buildenv.2009.01.013.
Liu, X., Huang, B., Li, R., Zhang, J., Gou, Q., Zhou, T., et al., 2022. Wind environment assessment and planning of urban natural ventilation corridors using GIS: Shenzhen as a case study. Urban Clim. 42, 101091. https://doi.org/10.1016/j.uclim.2022.101091.
Liu, S., Xu, L., Chen, B., Deng, Z., Li, P., Zhao, R., et al., 2025. Recent progress in optimization of RANS turbulence models for accurate urban airflow and contaminant dispersion simulations. Sustain. Cities Soc., 106336 https://doi.org/10.1016/j.scs.2025.106336.
Lu, X., Chen, L., Zhou, Y., Huang, Z., 2009. Shaking table model tests on a complex high-rise building with two towers of different height connected by trusses. Struct. Design Tall Spec. Build. 18 (7), 765–788. https://doi.org/10.1002/tal.460.
Lyu, K., Feng, S., Li, X., Wang, Q., Zhao, X., Yu, S., et al., 2022. SARS-CoV-2 aerosol transmission through vertical sanitary drains in high-rise buildings—Shenzhen, Guangdong Province, China, march 2022. China CDC Weekly 4 (23), 489. https://doi.org/10.46234/ccdcw2022.108.
Masson, V.J.B.-L.M., 2000. A physically-based scheme for the urban energy budget in atmospheric models. Bound.-Layer Meteorol. 94 (3), 357–397. https://doi.org/10.1023/A:1002463829265.
Merlier, L., Kuznik, F., Rusaouën, G., Salat, S., 2018. Derivation of generic typologies for microscale urban airflow studies. Sustain. Cities Soc. 36, 71–80. https://doi.org/10.1016/j.scs.2017.09.017.
Ministry of Housing and Urban-Rural Development of the People's Republic of China, 2025. Residential project code (GB 55038–2025). https://www.gov.cn/zhengce/zhengceku/202504/content_7016620.htm.
Montazeri, H., 2011. Experimental and numerical study on natural ventilation performance of various multi-opening wind catchers. Build. Environ. 46 (2), 370–378. https://doi.org/10.1016/j.buildenv.2010.07.031.
Nascimento, D., Ascenso, A., Lopes, D., Lopes, M., Rodrigues, V., 2025. CFD modelling of an urban microclimate during a heat wave: coupling solar radiation and heat transfer. Urban Clim. 62, 102486. https://doi.org/10.1016/j.uclim.2025.102486.
Nevers, C., Kubilay, A., Carmeliet, J., Derome, D., 2024. CFD simulation of the wind flow under lift-up buildings using a porous approach. Build. Environ. 263, 111867. https://doi.org/10.1016/j.buildenv.2024.111867.
Qiu, X., Zhou, J., Xiao, X., Zhu, W., Zhang, J., Gui, S., et al., 2023. The numerical simulation study of pumping airflow driven by wind pressure for single-and multi-room buildings. Buildings 13 (12), 3066. https://doi.org/10.3390/buildings13123066.
Ray, S.D., Gong, N.-W., Glicksman, L.R., Paradiso, J.A., 2014. Experimental characterization of full-scale naturally ventilated atrium and validation of CFD simulations. Energ. Buildings 69, 285–291. https://doi.org/10.1016/j.enbuild.2013.11.018.
Roache, P.J., 1997. Quantification of uncertainty in computational fluid dynamics. Annu. Rev. Fluid Mech. 29 (1), 123–160. https://doi.org/10.1146/annurev.fluid.29.1.123.
Sha, H., Qi, D., 2020. A review of high-rise ventilation for energy efficiency and safety. Sustain. Cities Soc. 54, 101971. https://doi.org/10.1016/j.scs.2019.101971.
Shetabivash, H., 2015. Investigation of opening position and shape on the natural cross ventilation. Energ. Buildings 93, 1–15. https://doi.org/10.1016/j.enbuild.2014.12.053.
Shirzadi, M., Mirzaei, P.A., Tominaga, Y., 2021. LES analysis of turbulent fluctuation in cross-ventilation flow in highly-dense urban areas. J. Wind Eng. Ind. Aerodyn. 209, 104494. https://doi.org/10.1016/j.jweia.2020.104494.
Tominaga, Y., Mochida, A., Yoshie, R., Kataoka, H., Nozu, T., Yoshikawa, M., et al., 2008. AIJ guidelines for practical applications of CFD to pedestrian wind environment around buildings. J. Wind Eng. Ind. Aerodyn. 96 (10−11), 1749–1761. https://doi.org/10.1016/j.jweia.2008.02.058.
Toparlar, Y., Blocken, B., Maiheu, B., van Heijst, G.J.F., 2017. A review on the CFD analysis of urban microclimate. Renew. Sust. Energ. Rev. 80, 1613–1640. https://doi.org/10.1016/j.rser.2017.05.248.
van Hooff, T., Blocken, B., 2010. Coupled urban wind flow and indoor natural ventilation modelling on a high-resolution grid: a case study for the Amsterdam ArenA stadium. Environ. Model Softw. 25 (1), 51–65. https://doi.org/10.1016/j.envsoft.2009.07.008.
van Hooff, T., Blocken, B., Tominaga, Y.J.B., Environment., 2017. On the accuracy of CFD simulations of cross-ventilation flows for a generic isolated building: comparison of RANS. LES Exp. 114, 148–165. https://doi.org/10.1016/j.buildenv.2016.12.019.
Yamamoto, T., Ozaki, A., Kaoru, S., Taniguchi, K., 2021. Analysis method based on coupled heat transfer and CFD simulations for buildings with thermally complex building envelopes. Build. Environ. 191, 107521. https://doi.org/10.1016/j.buildenv.2020.107521.
Yang, D., Du, T., Peng, S., Li, B., 2013. A model for analysis of convection induced by stack effect in a shaft with warm airflow expelled from adjacent space. Energ. Buildings 62, 107–115. https://doi.org/10.1016/j.enbuild.2013.02.045.
Younes, C., Abi Shdid, C., 2013. A methodology for 3-D multiphysics CFD simulation of air leakage in building envelopes. Energ. Buildings 65, 146–158. https://doi.org/10.1016/j.enbuild.2013.05.050.
Zaniboni, L., Albatici, R., 2022. Natural and mechanical ventilation concepts for indoor comfort and well-being with a sustainable design perspective: a systematic review. Buildings 12 (11), 1983. https://doi.org/10.3390/buildings12111983.
Zhai, Z.J., Johnson, M.-H., Krarti, M., 2011. Assessment of natural and hybrid ventilation models in whole-building energy simulations. Energ. Buildings 43 (9), 2251–2261. https://doi.org/10.1016/j.enbuild.2011.06.026.

Zhang, J., Lu, W., Huo, R., Feng, R., 2008. A new model for determining neutral-plane position in shaft space of a building under fire situation. Build. Environ. 43 (6), 1101–1108. https://doi.org/10.1016/j.buildenv.2007.02.004.

Zhang, X., Weerasuriya, A., Wang, J., Li, C.Y., Chen, Z., Tse, K., et al., 2022. Cross-ventilation of a generic building with various configurations of external and internal openings. Build. Environ. 207, 108447. https://doi.org/10.1016/j.buildenv.2021.108447.

Zhu, Y., Luo, M., Ouyang, Q., Huang, L., Cao, B., 2015. Dynamic characteristics and comfort assessment of airflows in indoor environments: a review. Build. Environ. 91, 5–14. https://doi.org/10.1016/j.buildenv.2015.03.032.